Review

An Overview of Physical Phenomena Involved in the Laser Powder Directed Energy Deposition Process

Gabriele Piscopo, Eleonora Atzeni, Abdollah Saboori and Alessandro Salmi *

Department of Management and Production Engineering (DIGEP), Politecnico di Torino, Corso Duca degli Abruzzi 24, 10129 Torino, Italy

* Correspondence: alessandro.salmi@polito.it; Tel.: +39-011-090-7263

Abstract: Laser Powder Directed Energy Deposition (LP-DED) is an Additive Manufacturing process in which a laser beam is used to generate a melt pool onto a substrate. The additional material, in form of powder material, is fed into the generated melt pool and a raised track is obtained. The LP-DED process is very powerful for different applications such as the repair operations and the production of functionally graded material, however the application is still limited and one of the main reasons is related to the lack of knowledge in the physics of the process mechanisms. The process is influenced by a huge number of parameters and three main mechanisms can be identified. These mechanisms are the powder flow, the generation of the molten pool and the solidification process and for each of these mechanisms the process parameters have a different relevance. In this paper, a review of the main mechanisms and the relationship between the process parameters and the outcome of each step of the process is presented.

Keywords: additive manufacturing; directed energy deposition; laser metal deposition; powder stream; melt pool; microstructure; residual stress

1. Introduction

Additive Manufacturing (AM) technologies were born in late 1980 as useful processes to produce prototypes faster and more economically than the conventional production system [1]. The basic idea of the AM processes is that a component, characterised by complex shapes, could be produced directly from a 3D model, depositing the material layer upon layer without using expensive tools or external equipment [2,3]. Nowadays considering the processes that use metal alloys as feedstock material, according to ISO/ASTM 52900:2021 [2], the main metal AM processes are Powder Bed Fusion (PBF) processes, that include Laser-Powder Bed Fusion (L-PBF) and Electron-Powder Bed Fusion (E-PBF), and Directed Energy Deposition (DED) processes. The graph which is shown in Figure 1 illustrates the number of metal AM systems that have been sold from 2003 to 2021 [4]. The graph refers to all the AM systems without distinguishing the process. It is possible to observe an abrupt increase in the number of systems sold from 2016 to 2018, and this number is expected to grow in the next years. This trend confirms the rising interest of the manufacturing industry in the AM processes [5].

The main PBF and DED systems are listed in Table 1, indicating the building volume. It is possible to observe that, despite PBF processes dominates the market [6], they can be used only to produce components with a maximum dimension of 400 mm. On the other hand, DED processes do not use a closed chamber and consequently the deposited dimension can reach up to 3000 mm in size. Another advantage of DED processes with respect to PBF processes is that an existing surface of a component could be used as a building platform. This characteristic is a very powerful feature for the repair application. Moreover, it is also possible to change the material during the deposition process, thus obtaining components characterized by different properties in different areas.

 doi:10.20944/preprints202211.0397.v1

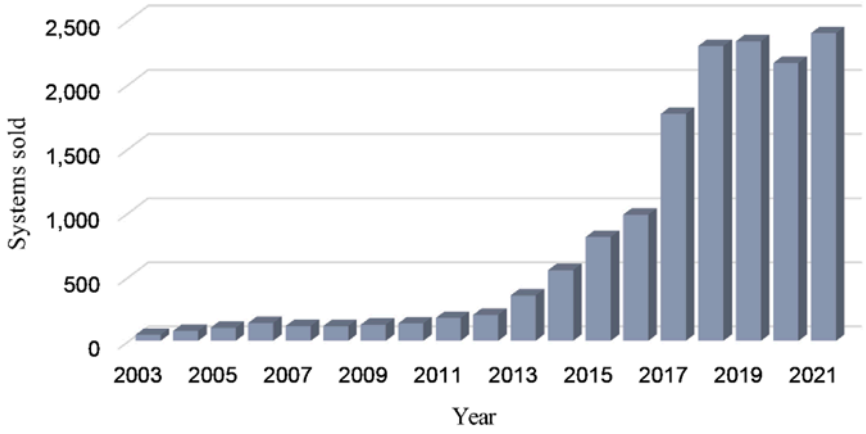

Figure 1. Metal Additive Manufacturing systems sold from 2003 to 2021 [4].

Table 1. Metal AM systems and their building volumes [7].

	System	Process name	Build volume (mm³)
PBF	GE Additive Arcam (A2x)	EBM	200 × 200 × 380
	GE Additive Arcam (Spectra H)	EBM	Φ250 × 430
	GE Additive Arcam (Spectra L)	EBM	Φ350 × 430
	EOS (M400)	DMLS	400 × 400 × 400
	Concept laser cusing (M2)	SLM	300 × 350 × 300
	MTT (SLM 250)	SLM	250 × 250 × 300
	Renishaw (AM 250)	SLM	245 × 245 × 360
	Realizer (SLM 250)	SLM	250 × 250 × 220
	Matsuura (Lumex Advanced 25)	SLM	250 × Φ250
DED	Optomec (LENS 850-R)	LENS	900 × 1500 × 900
	POM DMD (66R)	DMD	3200 × 3670 × 360°
	Accufusion laser consolidation	LC	1000 × 1000 × 1000
	Trumpf	LD	600 × 1000 long
	Sciaky (NG1) EBFFF	EBDM	762 × 483 × 508

DED processes can be classified regarding feedstock material and the energy source [8]. Among the different DED processes, the process that uses lasers as an energy source and powder as a feedstock material is the most commonly used [9], for this reason this review is focused on this proses. Different technologies that refer to the same process are developed and labelled differently, like Laser Metal Deposition (LMD), laser cladding, Laser Engineering Net Shaping (LENS®), Directed Light Fabrication (DLF), and Direct Metal Deposition (DMD™). In this work, the term Laser Powder Directed Energy Deposition (LP-DED) refers to this process.

In the LP-DED process, a deposition head delivers metallic powder into the melt pool generated by a focused laser beam. As a result of the localised thermal energy and rapid movement of the laser, an almost-instantaneous solidification of the molten material is obtained. The characteristics of the deposited part depend on a large number of parameters. According to Qi, *et al.* [10], up to 14 parameters can be identified that are laser power, laser beam diameter, spatial distribution, shielding gas flow rate, carrier gas flow rate, travel speed, powder feed rate, powder and building platform material properties, powder characteristics, powder feeding method, layer thickness, overlap percentage deposition strategy. These parameters define the mechanisms of the LP-DED process [11-13]. Three main mechanisms that can be identified are (i) the powder stream flow, (ii) the melt pool generation, and (iii) the solidification process. Moreover, during the process, complex interactions between the parameters are observed.

Preprints (www.preprints.org) | NOT PEER-REVIEWED | Posted: 22 November 2022 doi:10.20944/preprints202211.0397.v1

An in-depth description of the LP-DED process, which makes it possible to understand the physics of the process, must consider the mechanisms and process parameters that are closely related to each other. Figure 2 shows the three mechanisms of the LP-DED process and the relations between mechanisms, input parameters and outputs.

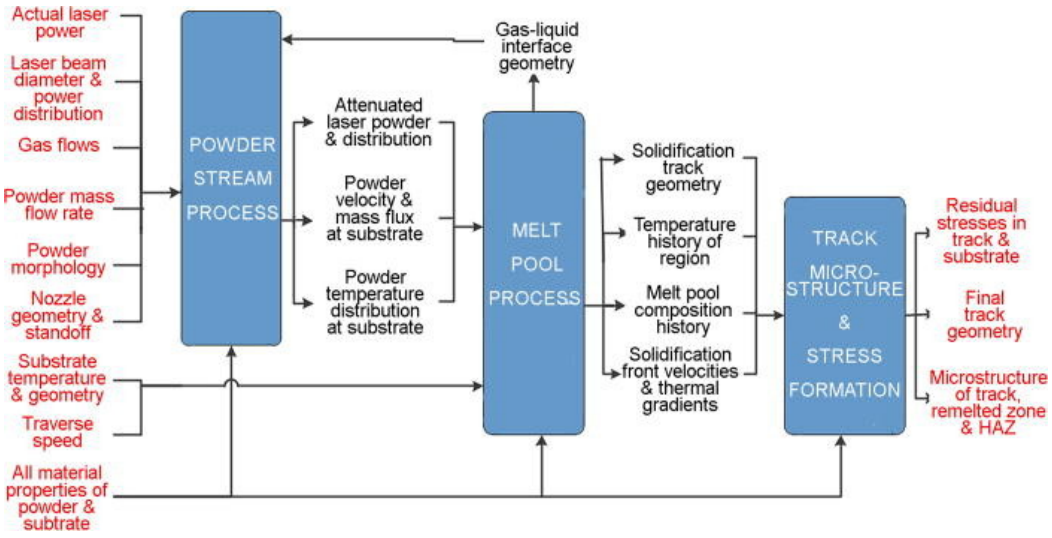

Figure 2. Subprocesses and process parameters describing the physics of the LP-DED process [12].

However, the process is generally analysed by considering each mechanism independently, and as a result, the interactions among the various process parameters are neglected. Therefore, a sequential approach is used to study the process, in which the output obtained as a result of each mechanism is used as an input variable for the following mechanism. Several reviews are available in the literature however most of them are focused on the application of the LP-DED process [6,14], on the modelling techniques [12], on the powder feed equipment [15,16], on the monitoring techniques [17] and on the feasibility of different alloys [18-22].

This work aims to describe the three mechanisms involved in the LP-DED process. At first, the powder flow process is described, in particular, the main results in terms of powder distribution and laser-powder interaction are highlighted. Then, the description is focused on the melt pool generation and the effect of process parameters on the temperature distribution into the melt pool. Moreover, the main forces acting in the melt pool and their influence on the melt pool morphology are analysed. Finally, the description is focused on the solidification process with a description of the resulting microstructure, the generation of residual stresses, and the analysis of the surface quality.

2. Powder stream

The study of the powder stream process is of fundamental importance as it defines the initial conditions for the generation of the melt pool [23,24]. In the LP-DED process, powders with a particle size between 30-150 μm are used [25]. Powders for AM can be mainly produced using three different technologies: Gas-Atomisation (GA), Water-Atomisation (WA), and Plasma Rotating Electrode Process (PREP) [26]. Powder particles produced by WA are characterized by an irregular shape elongated along a direction and dimpled surface textures [27,28]. Instead, powder particles produced by GA are characterized by a mainly spherical shape with smooth surface textures and some satellites [28,29]. Finally, powder particles produced by PREP are characterized by an extremely spherical shape without satellites or defects [30]. Figure 3 compares the morphology of 4130 steel powder produced via GA and WA, respectively.

 doi:10.20944/preprints202211.0397.v1

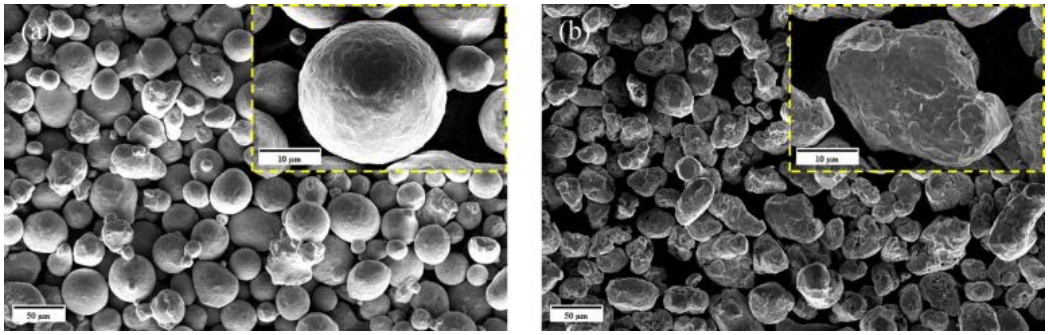

Figure 3. Morphology of 4130 steel powders obtained using the two systems: (**a**) gas-atomised and (**b**) water-atomised [31].

Different experiments were performed analysing the effect of powder production technologies on the characteristics of the produced parts. For instance, Pinkerton and Li [32] compared the effect of WA and GA 316L stainless steel powder on LP-DED walls. Results showed that although using the WA powder reduces the efficiency of the LP-DED process significantly, a finer microstructure and smoother surfaces are observed. As a consequence, WA powder can be considered a viable and more economical alternative for production [27]. Later, the same authors, during the deposition of WA and GA H13 tool steel powder, showed that using GA powders an higher value of deposition rate and an higher value of hardness were obtained [29,33]. Zhong, *et al.* [34] and Ahsan, *et al.* [35] compared the use of GA and PREP powder particles, respectively, for the production of IN718 and Ti6Al4V samples. They revealed a higher porosity content and a lower deposition rate on the tracks produced with the GA powders. Further improvements in the powder production methods could open new opportunities in production efficiency.

Figure 4. Deposition head configurations: (**a**) lateral configuration, (**b**) discrete coaxial configuration and (**c**) continuous coaxial configuration [11].

As stated earlier, the powder particles are driven by the deposition head to produce a powder stream that interacts with the melt pool generated by the laser. Therefore, it is evident the importance of the deposition head. The deposition head is mainly composed of laser optics, powder feed nozzles, shielding gas nozzles and sensors [9]. In general, different deposition head configurations have been developed so far [11]. The earliest deposition head is the lateral one (Figure 4a) that uses a single off-axis nozzle. However, using this type of deposition head faced with some limitations. The most important limit is that during the deposition process using this configuration, the geometry and the characteristics of deposited tracks are direction-dependent. To overcome this limitation, the coaxial configuration was introduced. Two types of coaxial deposition heads have been developed. The first one uses a discrete number of nozzles symmetrically located (Figure 4b), whereas, in the second one, a conical nozzle is used (Figure 4c). The coaxial deposition

 doi:10.20944/preprints202211.0397.v1

head configuration is the most used one [25] due to the high powder capture efficiency and the independence of the deposited tracks from the deposition direction [36]. However, it should be consider that the lateral deposition head is cheaper, due to the simplicity of the apparatus, moreover it is also possible to deposit into small location such as inside tubes and channels [9]. The configurations of deposition heads are illustrated in Figure 4. Table 2 summarises the main advantages and disadvantages of the different deposition head configurations.

Table 2. Advantages and disadvantages of deposition head configurations [36].

	Lateral	Discrete coaxial	Continuous coaxial
Pros	▪ Part accessibility ▪ Width of deposited track: 0.5-25 mm	▪ Unidirectional deposition ▪ Width of deposited track: 2-7 mm ▪ Applied laser power up to 5 kW ▪ Unrestricted 3D functionality ▪ Integrated protective gas feeding	▪ Unidirectional deposition ▪ Width of deposited track: 0.3-5 mm ▪ Applied laser power: up to 3 kW ▪ Powder capture efficiency: maximum 90% (diameter of powder gas jet in focus: minimum 400 mm) ▪ Integrated protective gas feeding
Cons	▪ Directional deposition ▪ Less powder efficiency ▪ Alignment between powder and laser beam ▪ No integrated protective gas feeding	▪ Restricted part accessibility ▪ Low powder capture efficiency (diameter of the powder-gas jet in focus: minimum 2.5 mm)	▪ Restricted part accessibility ▪ Gravity influence, no deposition for tilting angles higher than 20° because of the inhomogeneous powder density distribution

The powder stream could be analyzed considering two aspects: the powder flow and the interaction between the powder and the laser beam. The first one refers to study the dynamics and the distribution of powder stream; the second one analyses the phenomena that govern the temperature increment of the powder particles and the laser attenuation.

2.1. Powder flow

In order to optimise the LP-DED process, several studies have been performed to obtain an in-depth characterisation of the powder flow. Optimising and understanding the powder flow could improve the catchment efficiency, that is, the fraction of powder particles entering the melt pool [37]. In LP-DED process the catchment efficiency in relatively low, less than 30% with a huge amount of scattered powder [38]. As a consequence, increasing the catchment value causes an improvement of the overall process efficiency. Among the other parameters, such as powder velocity and surface tension, the catchment efficiency is mainly influenced by powder flow concentration and distribution [37,39]. Consequently, several studies have been performed to understand the factors that significantly affect the powder flow.

Lin [39] performed one of the first experimental studies on coaxial flow during the LP-DED process. In his work, image analysis and optical sensors were used to measure the distribution of the powder stream. Results showed a quasi-Gaussian distribution of powder flow in the radial direction. Later, Pinkerton and Li [40] developed a mathematical model to predict the spatial distribution of the powder flow obtained using a continuous coaxial nozzle. Their model was experimentally validated using optical and image analysis techniques. Results showed that two regions in the powder stream could be highlighted, one before merging to a single jet and another after this point. Before the merging point the powder flow was characterized by an annular distribution then, after merging point a Gaussian distribution was observed.

These concentration distributions, prior and in the merging point, were confirmed by Tabernero, *et al.* [41] using a Computational Fluid Dynamics (CFD) fluent model. However, the results experimentally validated using a technique based on selective weight

Preprints (www.preprints.org) | NOT PEER-REVIEWED | Posted: 22 November 2022 doi:10.20944/preprints202211.0397.v1

measuring, showed the presence of a transition zone, between the nozzle outlet and the merging point, with a non-uniform distribution (Figure 5).

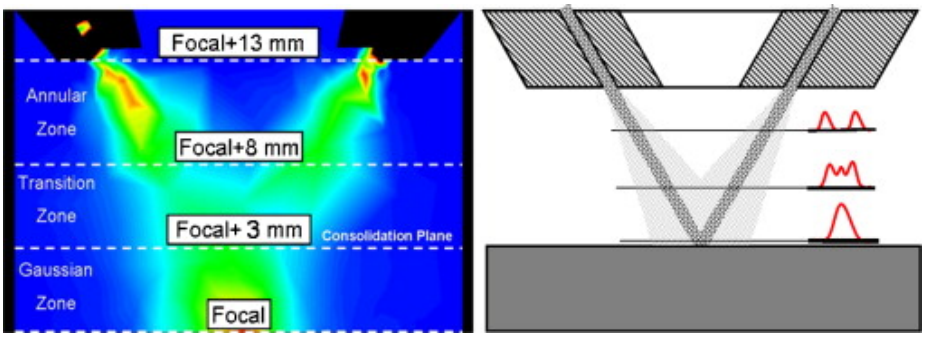

Figure 5. Evolution of powder flow distribution at different planes [41].

Later, contrary to what has always been assumed, Ibarra-Medina and Pinkerton [42] showed that the powder distribution close to the nozzle outlet above the stream focal point did not assume a uniform annular distribution, but it was possible to identify four concentration zones that correspond to the position of the nozzle inlets (Figure 6).

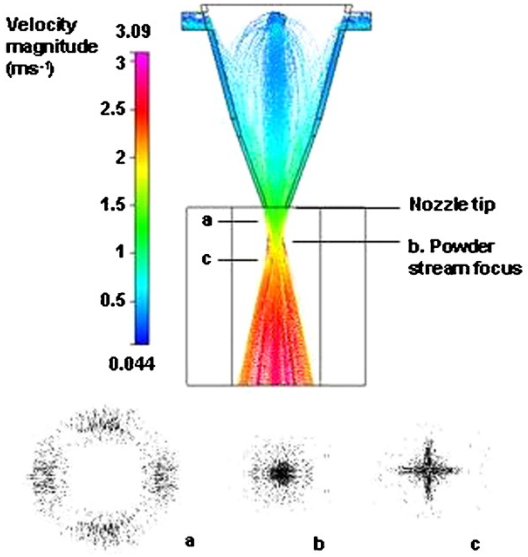

Figure 6. Modelled particles distribution and velocity obtained at different planes: (**a**) above the flow focal point, (**b**) at the flow focal point and (**c**) below the flow focal point [42].

As discussed above, the powder stream concentration distribution and its value vary along the axial direction (z-axis). The comparison between the numerical and the experimental results of powder concentration evaluated at different planes along the axial direction is reported in Figure 7. Wen, *et al.* [43] observed that prior the merging point, the powder concentration increased with the axial distance from the nozzle exit. Furthermore, the powder concentration peak moved close to the nozzle axis as the axial distance increased. Then, after focal point, the powder flow was characterised by a Gaussian distribution of powder concentration with a sharp reduction of peak concentration as the axial distance increases. The point in which the maximum concentration value is achieved corresponds to the focal point and it is located at a certain distance from the nozzle exit [44].

The position of the focal point and the concentration distribution strongly affect the catchment efficiency and the attenuation of the laser energy. Therefore, studies are focused on the evaluation of the effect of variables that influence the concentration distribution that are nozzle design, powder and gas flow rate and powder properties [45].

Preprints (www.preprints.org) | NOT PEER-REVIEWED | Posted: 22 November 2022 doi:10.20944/preprints202211.0397.v1

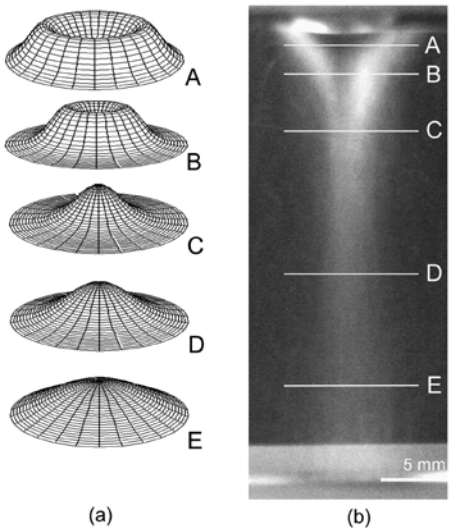

Figure 7. (**a**) Numerical and (**b**) experimental powders distribution evaluated at different planes below the nozzle exit [40].

In detail, the main geometrical characteristics of the nozzle that mainly influenced the powder flow behaviour are the nozzle configuration, the injection angle and the dimension of the channel at the outlet [39,40,45-49]. Lin [47] developed a two-dimensional numerical model in order to analyse the effect of the configuration of the deposition nozzle [47]. Using a continuous coaxial deposition head, a variation of powder concentration was obtained, varying the configuration of the inner nozzle. The configurations studied in his work are illustrated in Figure 8. Results highlighted that, using a configuration with an outward position of the inner nozzle (Figure 8a), the powder concentration value increased of about 50% compared to that obtained with the inner nozzle at the inward position. In addition, the author observed that the value of the concentration peak was highly influenced by the outer shielding gas velocity, but the axial position of the powder stream focus plane remained almost unaffected.

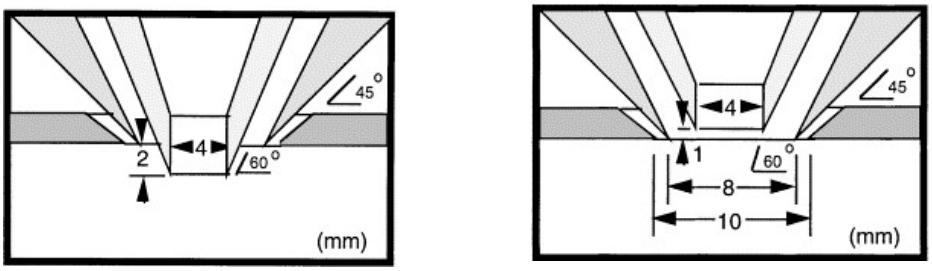

(**a**) (**b**)

Figure 8. Coaxial deposition head configurations: (**a**) outward and (**b**) inward nozzle position [47].

In general, it is observed that smaller dimension of the outlet leads to a smaller powder flow diameter in the focal point. For instance, Li, *et al.* [49] using a discreate coaxial deposition head with three nozzles showed that reducing the diameter of the nozzle from 2.0 mm to 1.0 mm, the concentration distribution diameter was reduced from 5.9 mm to 2.4 mm. A similar behavior was obtained by Ferreira, *et al.* [48] using a continuous coaxial deposition head. In addition to the outlet diameter, Li, *et al.* [49] showed that also the internal shape of the nozzles and their length influenced the concentration distribution and the position of the focal point with the best results obtained using straight and long channels. Then, it should be considered that a free, undisturbed powder flow differs significantly from a powder flow that impacts a surface [50,51]. Hence, the substrate and its distance from the deposition head play an important role [50]. The interaction between

Preprints (www.preprints.org) | NOT PEER-REVIEWED | Posted: 22 November 2022 doi:10.20944/preprints202211.0397.v1

substrate and powder flow was studied by Ibarra-Medina and Pinkerton [50] using a CFD analysis. They found that the substrate position strongly influenced the powder concentration. In particular, a higher concentration was obtained when the substrate was located very close to the nozzle (Figure 9).

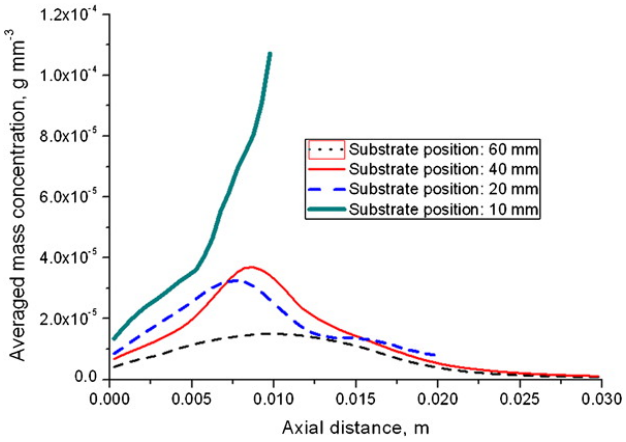

Figure 9. Effect of substrate position on particles concentration [50].

Another factor that affects the powder stream concentration and distribution is the velocity of the powder particles [52,53]. Ibarra-Medina and Pinkerton [42] showed that the collisions that occur inside the nozzle walls caused a reduction of the powder particles velocity. Then, during the in-flight time, powders increased momentum due to the effect of gases and an increase in velocity was observed. Beneath the nozzle, powder particles velocity (u_p) slightly increased, however, a wide speed range was observed with the fastest particles that had twice the speed of the slowest particles [54]. The powder particles velocity was also influenced by the interaction between powders and the laser radiation. In fact, it was observed that when the laser was switched on, the particles were characterised by higher speed [55,56]. This acceleration was related to the light-propulsion caused by the reaction between the material-vapour recoil with the beamed part of the particle [57]. In addition, Tan, *et al.* [58] showed that the average powder velocity increased with increasing the shielding gas flow rate. Moreover, Kovalev, *et al.* [54] showed a wide distribution of powder particles velocity was obtained as depicted in Figure 10. This wide velocity distribution was attributed to the complexity of phenomena that govern the gas-powder dynamics and the dispersion of powder size.

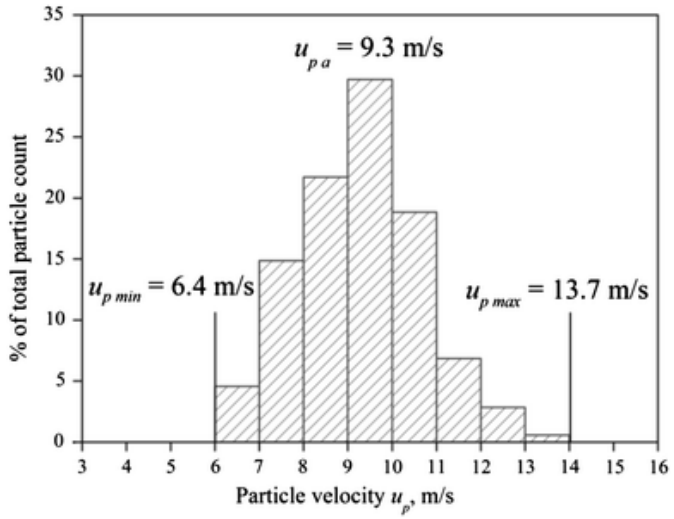

Figure 10. Distribution of particles velocities at a distance of 30mm below the nozzle exit [54].

Preprints (www.preprints.org) | NOT PEER-REVIEWED | Posted: 22 November 2022 doi:10.20944/preprints202211.0397.v1

The relationship between the powder stream process parameters and the corresponding flow is another important aspect that should be considered in the optimization of the powder flow. Kovalev, *et al.* [54] performed a theoretical and experimental investigation of powder flow resulting from a coaxial deposition of AISI 431 powder produced using water atomisation. They suggested that the optimal working area, where the coefficient of powder usage is maximised, was around the powder stream focal point. Hence, it is clear the importance of defining the powder focus plane. The relationships between powder flow characteristics, such as powder concentration and powder focus plane distance, and process parameters were investigated by Liu, *et al.* [59] using a numerical model based on the gas-solid flow. The peak of powder stream focal point and its position were significantly affected by the inner gas flow velocity. In particular, increasing the inner gas velocity, a reduction of the peak and an increase of the focal point axial distance were observed (Figure 11a). Moreover, it was observed that an excessive shielding gas flow led to a powder flow defocusing and, as a consequence, a reduction of the process efficiency [60]. The peak of powder concentration could be increased by increasing the powder feed rate [59]. From Figure 11b, it is also possible to observe that the focal point axial distance was unaffected by the powder feed rate. This result was experimentally confirmed by Tan, *et al.* [58] using a high-speed camera. Figure 12 shows the powder flow obtained with the observation method by varying the powder feed rate.

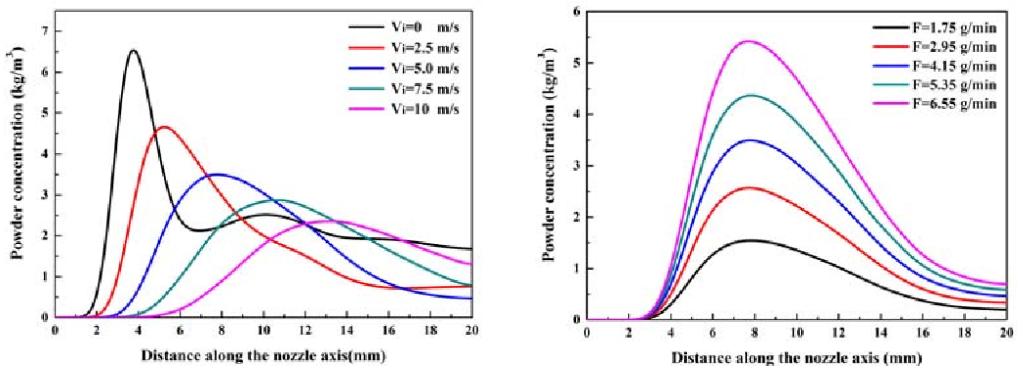

(**a**) (**b**)

Figure 11. Variation of particles concentration with (**a**) inner shielding gas velocity and (**b**) powder feed rate [59].

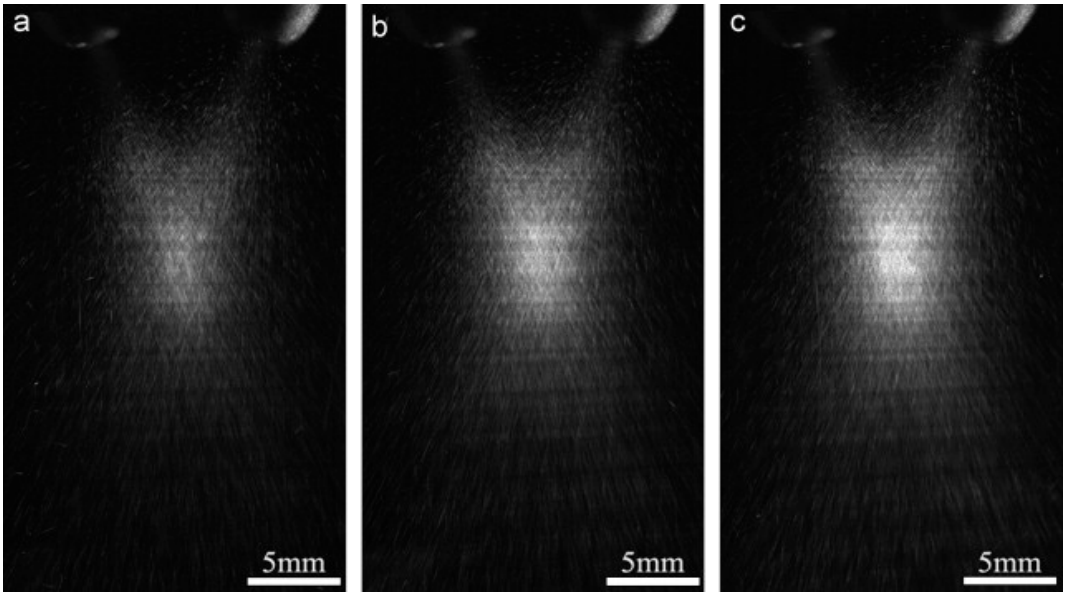

Figure 12. Powder distribution at different powder flow rates [58].

 doi:10.20944/preprints202211.0397.v1

In addition, the powder focus plane was also influenced by the material density [53]. In fact, Morville, *et al.* [61] used the Particle Tracing Module of Comsol Multiphysics ® to analyse the particle trajectory of two different materials that are 316L stainless steel and Ti6Al4V alloys. As depicted in Figure 13, both the analysed materials exhibited a convergent trajectory of the powder stream. However, the focus plane position with respect to the deposition head exit was obtained at a distance of 6.6 mm from 316L and at a distance of 9.9 mm for Ti6Al4V. This was related to the fact that the axial effect of the axial gas flow is less important on heavier particles, and consequently, the heavier powder particles reach the deposition head axis closer to the deposition head exit.

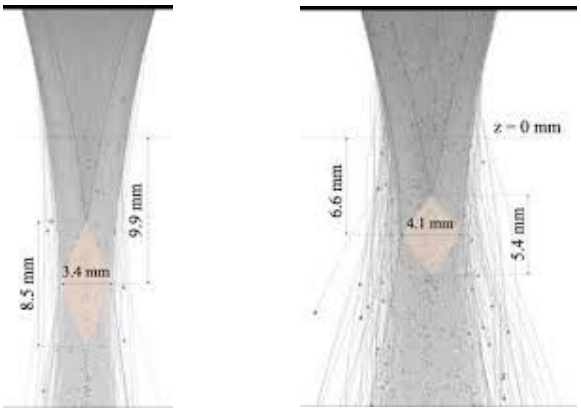

(**a**) (**b**)

Figure 13. Focal plane position for (**a**) Ti6Al4V and (**b**) 316L powder [61].

2.2. Powder heating and laser attenuation

One of the main characteristics of the LP-DED process is melting the powder particles when they enter the melt pool generated by the laser. Actually, the powder particles absorb energy during the in-flight time and their temperature increases. Under specific values of process parameters, the powder particles could melt during the in-flight time. However, to improve the adhesion to the substrate and the process's stability, this condition is typically avoided, and the process parameters are selected to melt only the substrate or previously deposited layers [9,62].

The increase of powder temperature during the in-flight time is caused by the interaction between powder and the laser beam. This interaction mainly depends on standoff distance, that is the distance between the deposition head and the substrate and powder particles velocity. The laser-powder interaction is governed by the electromagnetic and radiative properties of the powder particles and of the environment. Due to this interaction, besides the rise of powder temperature, the laser power is reduced by absorption, reflection and scattering of light by powder particles, resulting in an attenuation of the useful laser power [62,63]. Figure 14 gives a schematic illustration of phenomena that occurs during laser-powder interaction.

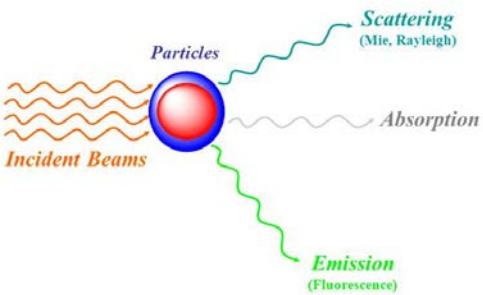

Figure 14. Illustration of the effects occurring during the laser-powder interaction

Preprints (www.preprints.org) | NOT PEER-REVIEWED | Posted: 22 November 2022 doi:10.20944/preprints202211.0397.v1

One of the first analyses of powder heating was performed by Lin [64] using a mono-dimensional analytical model. He showed that powder temperature highly depends on inner gas velocity and laser power. For example, increasing the gas flow velocity from 2 m/s to 6 m/s, a variation of about 700 °C of powder temperature was observed. The model outcome was compared with experimental results obtained using a pin-hole photodetector, and good agreement was obtained. The experimental results showed that the powder particles temperature inside the stream varied by about 500 °C due to the particle size distribution on the powder stream.

Transient heat transfer phenomena occur when powders interact with the laser beam. These phenomena are essentially conduction, convection and radiation. The increment of powder temperature is usually calculated by means of an energy balance. An important parameter that allows studying the powder heating is the Biot number [65] defined as $B_i=h_cL_p/k_p$ where h_c is the convection coefficient, L_p is the characteristic length (for a spherical particle with a radius of r_p, $L_p=r_p/3$), and k_p is the thermal conductivity of the material. When $B_i<<1$, as in the majority of cases during the LP-DED process, the temperature gradient within each powder particle is negligible [42,66]. Under this condition, the lumped capacitance method can be applied, and the energy balance can be described using the following equation:

$$V_p\rho_p c_p\frac{dT}{dt}=I_p\eta_p\pi r_p^2-h_c(T-T_\infty)4\pi r_p^2-\varepsilon_r\sigma(T^4-T_\infty^4)4\pi r_p^2 \quad (1)$$

where V_p is the particle volume, ρ_p is the particle density, c_p is the particle specific heat, T is the actual temperature of the particle at the time t, I_p is the incident energy on the particle, η_p is the particle absorptivity, h_c is the convection coefficient, ε_r is the radiation coefficient, σ is the Stefan-Boltzman constant and T_∞ is the temperature of the shielding gas.

Ibarra-Medina and Pinkerton [42] analysed the interaction between the laser beam and the powder particles. Figure 15 shows the comparison between numerical and experimental powder temperature increment with respect to in-flight distance for different laser power values. Comparing the curves, the authors showed that the model allows analysing the temperature increment during the process from a qualitative point of view.

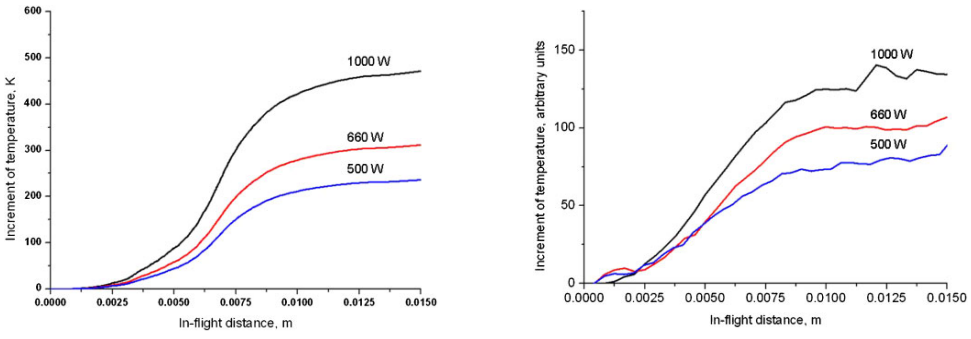

(**a**) (**b**)

Figure 15. (**a**) Numerical and (**b**) experimental powders temperature increment at different values of laser power [42].

Several authors then successfully applied the lumped capacitance method combined with a different solution approach. Pinkerton [46] solved Eq. (1) analytically and reported that powder was characterised by different temperatures within the flow due to the different trajectories. In the focus plane, the maximum temperature was reached at the centre of the laser beam, whereas below the focus plane, a uniform temperature distribution along the radial position was observed.

Preprints (www.preprints.org) | NOT PEER-REVIEWED | Posted: 22 November 2022 doi:10.20944/preprints202211.0397.v1

In order to avoid the complex radiation problem involved in laser-powder interaction, different methods were used to study the power attenuation caused by the powder stream. The most used methods are:

- the Hagens-Rubens relationship;
- the Bramson's equation;
- the use of the Beer-Lambert attenuation model.

Using the Hangens-Rubens relationship, defined by Eq. (2) or Bramson's equation, described by Eq. (3), a time-space-temperature averaged coefficient is obtained to estimate the laser attenuation. However, it should be noted that these relations do not consider the powder feed rate. Typical values obtained for an Nd-YAG laser are 0.36 for Inconel 718 [67] and 0.28 for 316L stainless steel [68]. The laser-surface coupling coefficient, $A(T)$, and the absorption coefficient, η, are defined using the following equation:

$$A(T) = [8\varepsilon_0 \omega \rho_e(T)]^{1/2} \quad (2)$$

$$\eta = 0.365\left(\frac{\rho_e}{\lambda}\right)^{1/2} - 0.067\left(\frac{\rho_e}{\lambda}\right) + 0.006\left(\frac{\rho_e}{\lambda}\right)^{3/2} \quad (3)$$

where ε_0 is the permittivity of free space, ω is the angular frequency of the laser irradiation, $\rho_e(T)$ is the material temperature-variant electrical resistivity, and λ is the wavelength of the laser beam.

Using the Beer-Lambert attenuation model, the radial distribution of the attenuated laser beam intensity at a distance z from the nozzle could be estimated as:

$$I'(r,z) = I_0(r)\, exp(-\sigma_{ext} N z) \quad (4)$$

where $I'(r,z)$ is the attenuated laser beam intensity, $I_0(r)$ is the initial laser beam intensity, σ_{ext} is the powder extinction coefficient, and N is the number of powder particles in a unit volume. N is proportional to the powder feed rate [62]. He and Mazumder [69] observed that by increasing the powder feed rate, a greater value of laser beam absorption was obtained, and consequently, a lower value of useful laser power was observed (Figure 16).

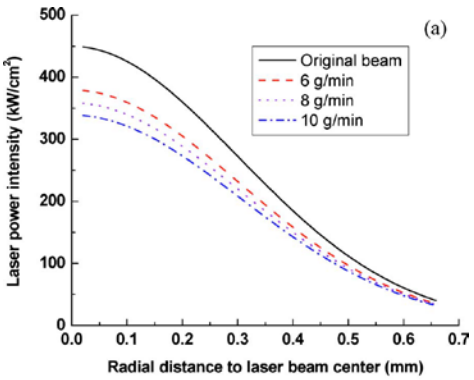

Figure 16. Resulting laser power intensity at different values of powder feed rate [69].

Evaluation of the laser absorption and, therefore, the absorption coefficient was also performed using experimental tests. Unocic and DuPont [70] used a Thermonetics Seebeck envelope calorimeter to estimate the process efficiency during the deposition of H13 tool steel powder on a substrate of the same material and copper powder deposited on an H13 tool steel substrate. Varying the laser power between 125 and 500 W and the powder feed rate between 0.08 and 0.33 g/s, they found that the efficiency ranges between 0.3 and 0.5. Using the same experimental setup, Sears [71] showed that process efficiency was about 0.42 during the deposition of Ti-6Al-4V onto a Ti-6Al-4V substrate and about 0.34 depositing 316L stainless steel powder onto a 304L stainless steel substrate. Peyre, *et al.* [72] showed that the attenuation slightly increases by increasing the powder feed rate.

Preprints (www.preprints.org) | NOT PEER-REVIEWED | Posted: 22 November 2022 doi:10.20944/preprints202211.0397.v1

3. Melt pool generation

The laser power available at the substrate, that is the power not attenuated by the powder flow is focused in a small area and causes a local increase of the temperature of the building platform and a melt pool is generated [73]. A schematic illustration of melt pool generation and the addition of material is depicted in Figure 17a. When the powder comes into the melt pool, it melts very quickly, and a raised track is obtained due to the material addition [11]. Typically, the melt pool generated during the LP-DED process is characterised by dimensions from 0.25 to 1 mm in width, 0.25 to 0.5 in height and 0.1 to 0.5 mm in depth [9,74]. During melt pool generation, thousands of degrees can be reached in a few milliseconds, and temperature value and distribution depend on several factors such as laser power, laser beam diameter, building platform material and travel speed [75]. Figure 17b shows the thermal image acquired by a 12-bit digital charge-couple device camera of a moving melt pool and the corresponding temperature obtained during a 316L stainless steel thin wall deposition.

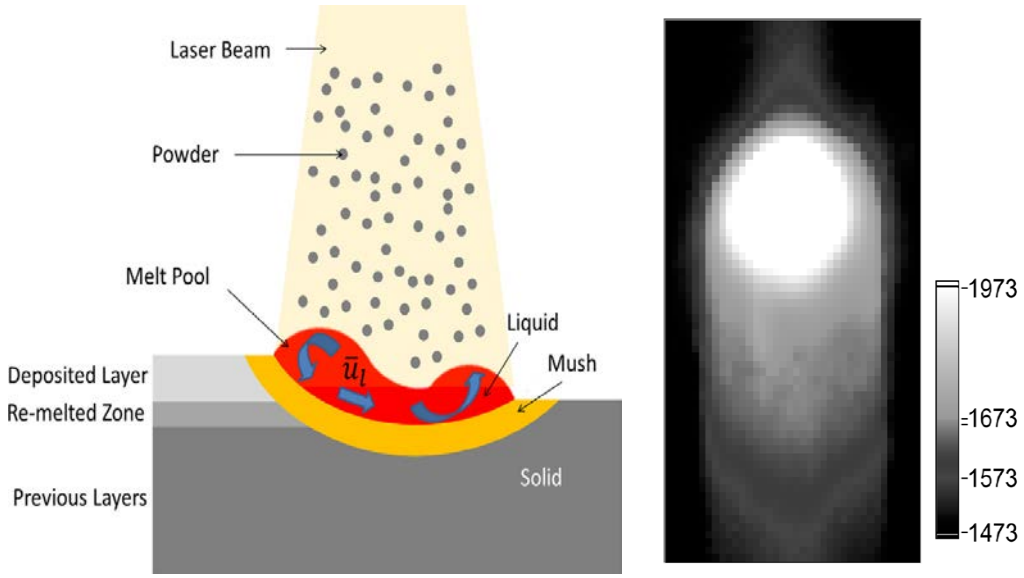

Figure 17. (a) Schematic representation of the melt pool generation [62] and (b) top view thermal image captured during the deposition of 316L thin wall [74].

Since the melt pool generation is the starting point of the solid track formation, its study is of fundamental relevance to optimise the building conditions [12,62,76]. Hence, it is important to understand which parameters have the most significant impact on the melt pool and how the melt pool dynamics affect the heat transfer. The equations governing the melt pool generation and the thermal behaviour are summarised in this paragraph.

The energy available at the substrate, which generates the melt pool and overheats the molten material, can be estimated using the following equation [62,77,78]:

$$I'' = I_L - I_{loss} \quad (5)$$

where I'' is the useful heat flux at the substrate, I_L is the heat flux at the substrate provided by the laser beam, and I_{loss} is the heat loss at the melt pool-vapour interface.

Assuming a Gaussian distribution of the heat source I_L can be expressed as [62]:

$$I_L = \frac{2 \times \eta \times P}{\pi r_L^2} exp\left(\frac{-2 \times r^2}{r_L^2}\right) \quad (6)$$

where P is the laser power, r_L is the laser beam radius, η is the absorption coefficient, and r is the radial distance from the laser beam centre.

Preprints (www.preprints.org) | NOT PEER-REVIEWED | Posted: 22 November 2022 doi:10.20944/preprints202211.0397.v1

The heat loss at the melt pool interface includes convection, radiation and vaporisation, and it is described by the following equation:

$$I_{loss} = h_c(T(r) - T_\infty) + \varepsilon_r \sigma(T^4(r) - T_\infty^4) + \rho_L \left|\frac{\Delta r}{\Delta t}\right|_e L_v \quad (7)$$

where the first term on the right side of the equation corresponds to the heat loss due to convection, the second term corresponds to the heat loss by radiation, and the last term represents the heat loss due to vaporisation of the melt pool. Therefore, in Eq. 7, h_c is the convection coefficient, $T(r)$ is the temperature at the position r, ε_r is the emissivity, σ is the Stefan-Boltzmann constant, ρ_L is the liquid density, L_v is the latent heat of vaporisation and $|\Delta r/\Delta t|_e$ is the topology deformation rate due to evaporation. The topology deformation rate due to evaporation can be estimated as [78]:

$$\left|\frac{\Delta r}{\Delta t}\right|_e = c_{sound}\, exp\left(-\frac{\overline{L_v}}{T(r)}\right) \quad (8)$$

where c_{sound} is the sound velocity in the material and $\overline{L_v}$ is the energy of evaporation per Avogadro's number.

3.1. Thermal behaviour

The incident laser beam heats the building platform locally. The laser heat flux superheats the material, and the obtained temperature in the melt pool is largely above the melting temperature of the material [68]. For instance, Hofmeister, *et al.* [79] showed that during the deposition of a 316L thin wall, the molten pool temperature reached the value of about 2000 K, which is 25% higher than the melting temperature of 316L. Melt pool shape and dimensions depend on the laser beam intensity distribution [80], on the resulting temperature distribution and on the maximum temperature reached into the material. So, it is evident that the temperature value and its distribution are key parameters that significantly affect the melt pool. Griffith, *et al.* [81], during the deposition of a 316L thin wall, showed that the maximum temperature was obtained at the centre of the laser beam and then linearly decreased until the solidification temperature (1650 K) at a distance of around 2 mm from the centre, as represented in Figure 18.

Among the other process parameters, at the present time, it is consolidated that the process parameters that mostly affect the temperature distribution and consequently the melt pool dimensions [12] are the powder feed rate (Q), the travel speed (v) and the laser power (P) [9,12,82]. In the following paragraphs the effect of these parameters on the width, on the height and on the depth of the melt pool has been described.

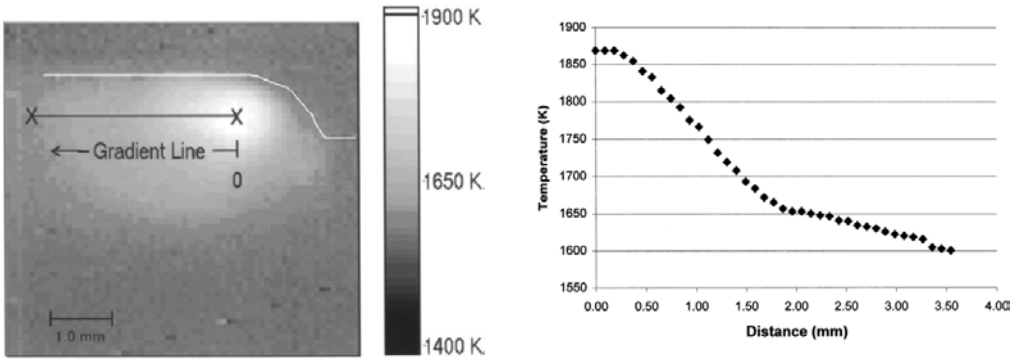

(**a**) (**b**)

Figure 18. (**a**) Digital image of the working area during the deposition of 316L thin wall and (**b**) temperature distribution measured across the gradient line (right) [81].

 doi:10.20944/preprints202211.0397.v1

3.1.1. Effect of laser power

Currently, it is globally accepted that by increasing the laser power, a higher temperature of the melt pool is achieved. Figure 19 showed the temperature distribution in the direction perpendicular to the travel speed for different laser power values. It is possible to observe that, during the deposition of Ti6Al4V alloy, increasing the laser power from 2 kW to 5 kW the maximum temperature increased from 1400 °C to 1850 °C and therefore an enlarged melt pool width is obtained [72,83-88].

However, contradictory results were obtained in the literature by analysing the effect of laser power on the melt pool height. Pinkerton and Li [33] and Peyre, *et al.* [72] showed that the layer height remained constant by varying laser power values. Srivastava, *et al.* [85] observed that a reduction of layer height was obtained by increasing the value of laser power. In contrast, Lee, *et al.* [86] and Pinkerton and Li [88] showed that layer height increases with laser power.

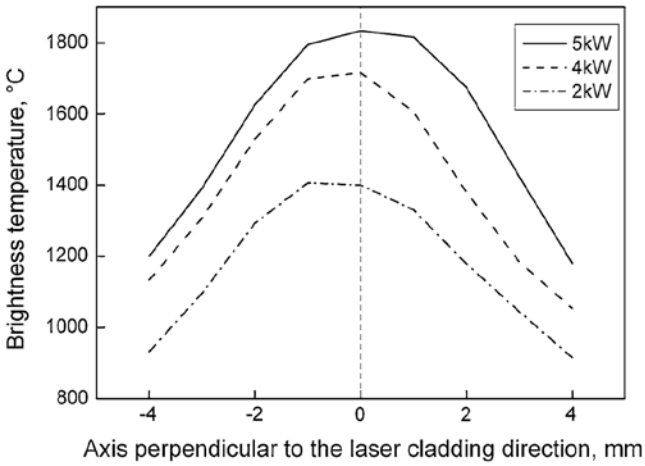

Figure 19. Effect of laser power on average temperature distribution into the melt pool [89].

3.1.2. Effect of powder feed rate

The powder feed rate represents the amount of additional material introduced in the deposition area. In the literature, there are contradictory results on the effect of powder feed rate on melt pool width. Pinkerton and Li [33], Lee, *et al.* [86] and El Cheikh, *et al.* [90] by varying powder feed rate, demonstrated that layer width was not influenced by this parameter. During the deposition of Ni20 powder on 316L substrate, Hua, *et al.* [83] showed that the melt pool temperature decreased with increasing the powder feed rate, as depicted in Figure 20. Therefore, it was found that by increasing the powder feed rate, a smaller melt pool area was obtained [91]. The reduction of melt pool dimensions was confirmed by Srivastava, *et al.* [85] during the production of Ti-48Al-2Mn-2Nb rectangular strips. The reduction in melt pool with was attributed to the increasing of laser attenuation due to the increasing of powder feed rate. Conversely, Hu, *et al.* [84] and Peyre, *et al.* [72] observed that the melt pool width slightly increased with the powder feed rate. Consequently, the effect of powder feed rate on melt pool width is highly dependent on the value of laser power and it could not be studied independently [82].

On the other hand, the layer height linearly increases with increasing the powder feed rate [33,84,86,92-94]. Srivastava, *et al.* [85] observed that the layer height increased for low values of powder feed rate; however, after a critical value increasing the powder feed rate, a reduction of layer height was observed. However, it should be considered the existence of an upper limit of the powder feed rate that depends on the melt pool dimension. If the powder feed rate exceeds this value, the incoming particles bounce on the particles in the melt pool, creating the Self-Shielding Effect [95].

Preprints (www.preprints.org) | NOT PEER-REVIEWED | Posted: 22 November 2022 doi:10.20944/preprints202211.0397.v1

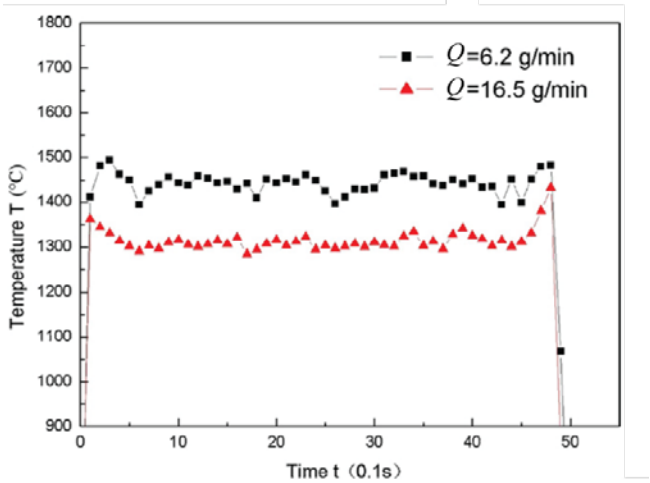

Figure 20. Effect of powder feed rate on temperature measurements using thermal monitoring [83].

3.1.3. Effect of travel speed

The temperature distributions measured at the centre of the melt pool at different travel speeds are reported in Figure 21 [83]. It is possible to observe that by increasing the travel speed, a huge reduction of the temperature was obtained. Accordingly, by increasing the travel speed, a smaller melt pool width is expected.

Yellup [87] showed that for low laser power values, the layer width decreased slightly by increasing the travel speed (Figure 22). This decrement was confirmed by Hu, *et al.* [84], Wu, *et al.* [93], Pinkerton and Li [33],Srivastava, *et al.* [85] and Lee, *et al.* [86]. However, at a high level of laser power, the dimension of layer width was not significantly affected by the travel speed [87]. Hu, *et al.* [84] observed that after a critical value of travel speed, the layer width was unaffected by the variation of process parameters and was equal to laser beam diameter. This behaviour indicates that also in this case it is not possible to consider the travel speed as an independent parameter, but it is advisable to indicate the power level of the laser to which it refers.

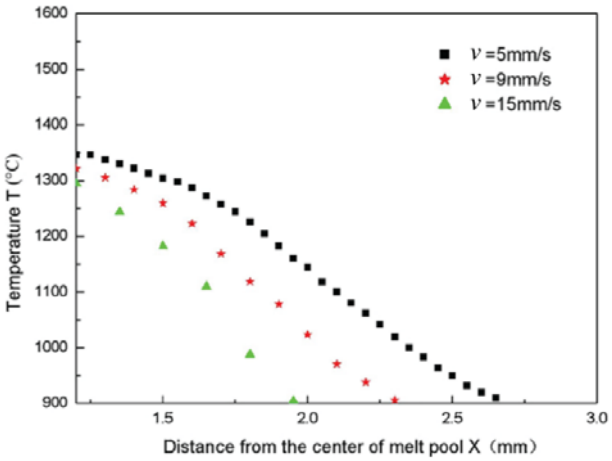

Figure 21. Effect of travel speed on temperature distribution along melt pool [83].

Hu, *et al.* [84], Wu, *et al.* [93] and Pinkerton and Li [33] observed that the layer height was inversely proportional to the travel speed. Yellup [87] and Srivastava, *et al.* [85] showed that before a critical value, the layer height increased by increasing the travel speed. After this critical value, a decreasing trend was observed, increasing the travel speed. The critical value depends on the material, the laser power and the z-increment of the deposition head.

Preprints (www.preprints.org) | NOT PEER-REVIEWED | Posted: 22 November 2022 doi:10.20944/preprints202211.0397.v1

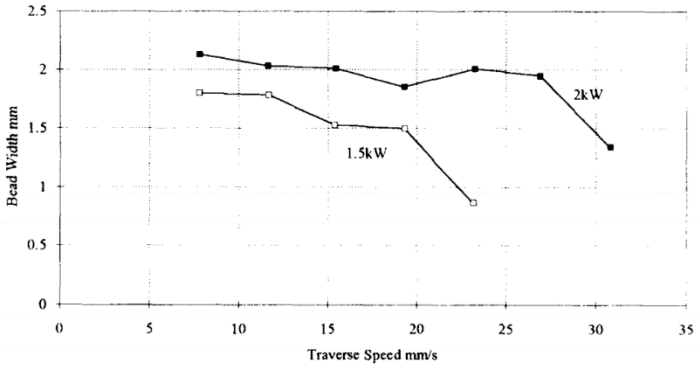

Figure 22. Variation of track width with respect to the travel speed varying the laser power [87].

3.2. Forces within the melt pool

In general, it is reported that the morphology and shape of a melt pool are mainly determined by the forces and the flows within the melt pool itself [96-98]. Two main types of forces that can be recognised are the buoyancy forces and the Marangoni forces [25,99,100]. The metal liquid flow caused by the buoyancy forces is illustrated in Figure 23a. The material density differences cause the buoyancy forces due to the temperature gradient into the melt pool. Indeed, the temperature in the melt pool is higher in the centre, and it reduces progressively near the boundary. As a consequence, the density of the metal melt pool increases from the centre (point a) to the border (point b) [99]. The Marangoni forces cause the Marangoni flows, also named surface tension-driven or thermocapillary convection. These flows are caused by surface tension gradients. The Marangoni number (*Ma*) is often used to measure the magnitude of Marangoni flows, and it is defined as [96]:

$$Ma = -\frac{\partial \gamma}{\partial T}\frac{1}{\mu \kappa} t_{mp} \nabla T \quad (9)$$

where $\partial\gamma/\partial T$ is the surface tension temperature coefficient, μ is the dynamic viscosity, κ is the thermal diffusivity, t_{mp} is the melt pool thickness on the surface and ∇T is the temperature gradient.

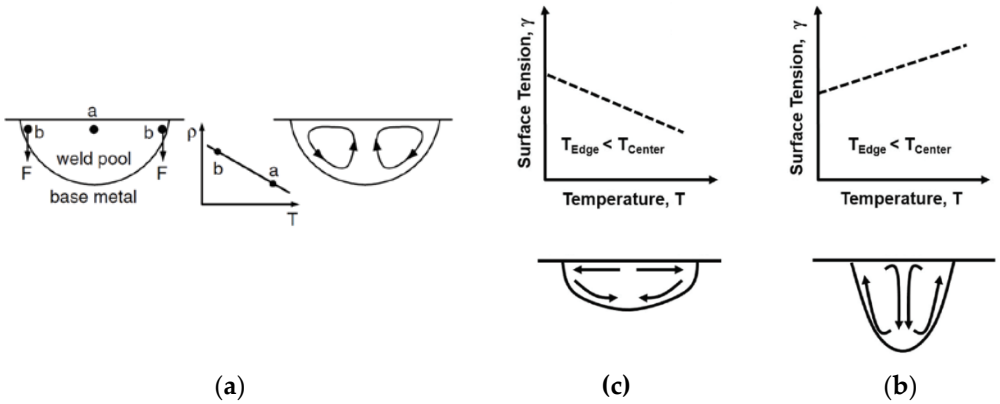

(**a**) (**c**) (**b**)

Figure 23. (**a**) Buoyancy forces and flows caused by the material density differences due to the temperature gradient [99]. Marangoni flows caused by the surface tension gradients: (**b**) a negative value of surface tension temperature coefficient causes a wide and shallow melt pool morphology instead (**c**) a positive value of surface tension temperature coefficient causes a deep and narrow melt pool morphology [101].

Comparing the magnitude of the flows acting into the melt pool, it is possible to observe that Marangoni flows dominate the melt pool behaviour [25,96,97] and for this reason the majority of the works are focused on that type of flow. The effect of Marangoni

 doi:10.20944/preprints202211.0397.v1

flows on the melt pool shape was numerically investigated by several authors [96,100,102,103], and the effect of surface tension gradient on melt pool flows is illustrated in Figure 23. It was showed that with a negative surface tension temperature coefficient value (Figure 23b), the melt pool flows were directed from the centre to the edge, and a wide and shallow melt pool morphology was obtained. On the other hand, the melt pool became deep and narrow with a positive value of surface tension temperature coefficient. Usually, the value of surface tension decreases as the temperature increases, so a negative value of the surface tension temperature coefficient is obtained [99]. However, the presence of surface-activant elements such as sulphur and oxygen changes the value of the surface tension temperature coefficient from negative to positive [25]. Nevertheless, Marangoni flows occur only below a critical travel speed [104]. Above this critical speed, the interaction time is too low, and the surface-tension gradients are avoided. For a 316L stainless steel, the critical velocity is on the order of 90 mm/s.

4. Solidification process

In general, high heating/cooling rates, marked temperature gradients, and increased bulk temperature involved in the LP-DED process are the key factors that define the thermal history of a component. This complex thermal history in part produced via the LP-DED process results in a non-equilibrium solidification which is also known as rapid solidification. This process which is characterised by a high solidification rate can offer several advantages such as the extension of solid solubility, precipitation of non-equilibrium or metastable crystalline phases, microsegregation free solidification, and formation of a cellular structure with non-equilibrium morphologies, in particular in the stainless steel alloys [105,106]. It is well documented that this complex thermal history and the solidification process, as explained earlier, determine the final microstructure and, consequently, the performance of the produced parts. For this reason, in the following section, the aim is to provide an overview of the microstructure, residual stress, and surface quality of metallic materials processed via the LP-DED process.

4.1. Microstructure

In the LP-DED process, morphology and grain size as the main microstructural features can be significantly influenced by the thermal history of the component during the building process. In general, it is reported that the cooling rate and thermal gradient can substantially define the thermal history of a part. However, it is well documented that there are lots of process parameters/variables that significantly affect the thermal history of the LP-DED parts. Therefore, this complex correlation between the process variables/parameters and thermal history makes the prediction of the microstructural features of LP-DED components very challenging. Nonetheless, in order to produce LP-DED parts with superior mechanical properties, it is very important to overcome this challenge and establish effective control mechanisms.

In the literature, several works have been studied the role of specific parameters on the microstructure and performance of the LP-DED parts with specific shapes [106-108]. However, in most of these works, the investigations have been carried out on the samples with simple geometries such as cubes and blocks. In contrast, in the case of complex shape components that can experience various thermal histories in different parts, it is not clear how to apply the outcomes of these investigations. In the literature, it is reported that the as-built microstructure depends mainly on the solidification rate within the melt pool, the cooling rate/temperature gradient ratio (R), the thermal gradient at the solidification front (G) [109,110]. G/R and $G \times R$, which is also known as cooling rate, are the two critical solidification parameters that influence the shape of the solidification front and the dimensions of the microstructure, respectively [111,112]. Columnar (elongated grain morphology), columnar-equiaxed, and equiaxed are the main structure morphology that can be achieved at different G and R values. Figure 24 shows the effects of G and R values on the

Preprints (www.preprints.org) | NOT PEER-REVIEWED | Posted: 22 November 2022 doi:10.20944/preprints202211.0397.v1

solidified microstructure. As can be seen, the columnar to equiaxed transition can be achieved at very high solidification rates, whereas, at high cooling rates, a finer microstructure can be obtained in the ab-built LP-DED parts. It should be highlighted that the optimum *G* and *R* values can be determined by different factors like materials properties, machine condition, part geometry and process parameters.

In general, in the LP-DED process, the cooling rate value ranges from 5×10^2 to 5×10^5 K/s [9,11,113]. The high cooling rate values, as discussed earlier, could lead to several advantages such as suppression of solid-state transformation, formation of non-equilibrium phases and very fine microstructures [9].

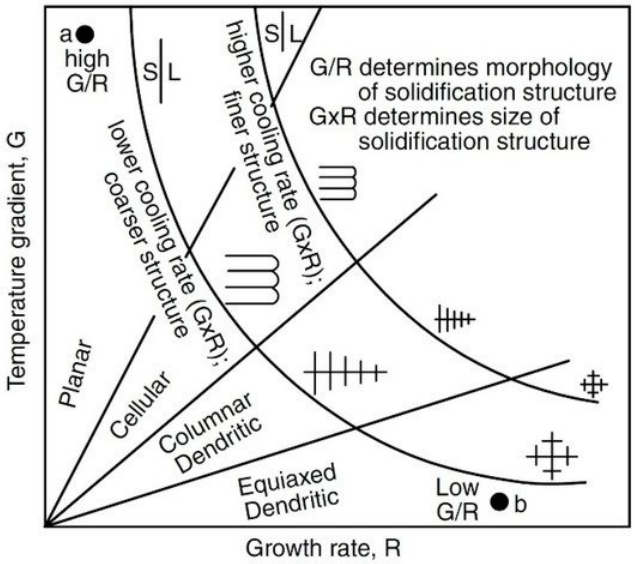

Figure 24. Effect of the temperature gradient and the solidification rate on the solidification microstructures and grain dimension [112].

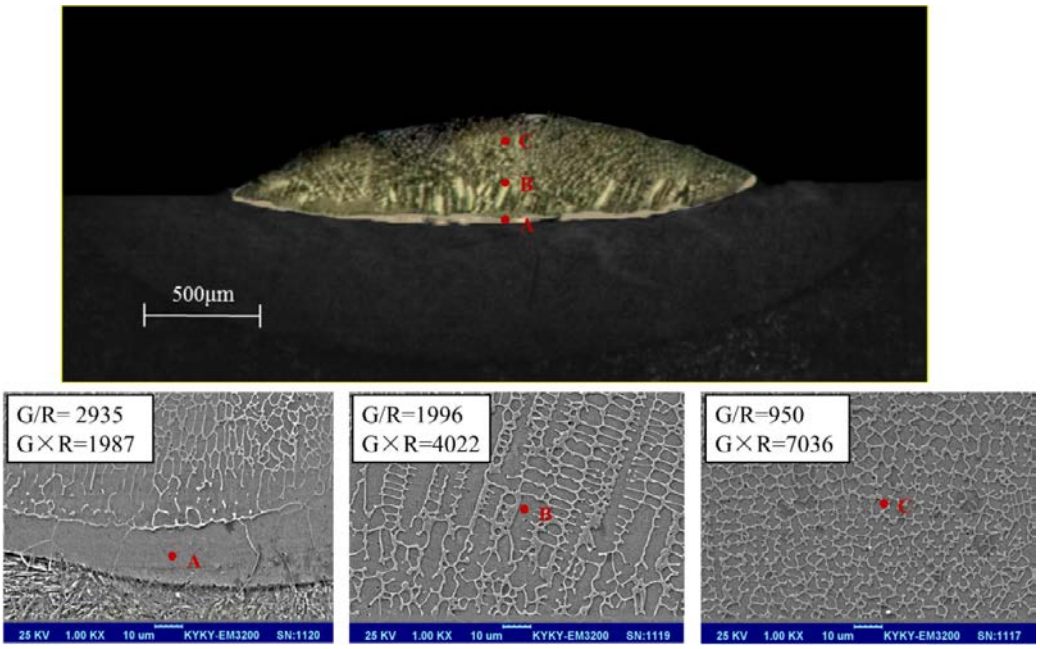

Figure 25. Experimental analysis of microstructure formation during the deposition of a single scan of Co-based alloy on steel. At the bottom of the deposited track (point A), a coarse planar front is observed. In the centre of the track (point B), columnar and coarse dendrite structures are observed. At the top of the track (point C), equiaxed and finer dendrites are obtained [114].

Preprints (www.preprints.org) | NOT PEER-REVIEWED | Posted: 22 November 2022 doi:10.20944/preprints202211.0397.v1

The $G \times R$ value at the bottom of the deposited track is very low, and then increases rapidly with the track height to reach its maximum value of about the travel speed, near the free-surface of the melt pool. On the other hand, the maximum value of G/R is obtained at the bottom of the melt pool and decreases approaching the melt pool free surface. As a consequence, a planar coarse microstructure is frequently obtained at the bottom of the deposited track and evolves to cellular, dendritic or equiaxed structures in the upper regions. The microstructure distribution is clearly visible in Figure 25 which shows the microstructural evolution that occurs during the deposition of a single track of Co-based alloy on steel.

Previous works have reported that epitaxial grain growth in the direction of maximum thermal gradient is the common mechanism in most metallic materials such as stainless steel [ref], titanium alloys [115,116], etc. However, for instance, in different LP-DED titanium components, various prior beta grain morphologies were revealed. For example, in a near beta titanium alloy (Ti-5Al-5Mo-4V-1Cr-1Fe), a "bamboo-like" grain morphology was detected in the building direction, which is a mixture of small columnar and equiaxed grains (Figure 26) [117].

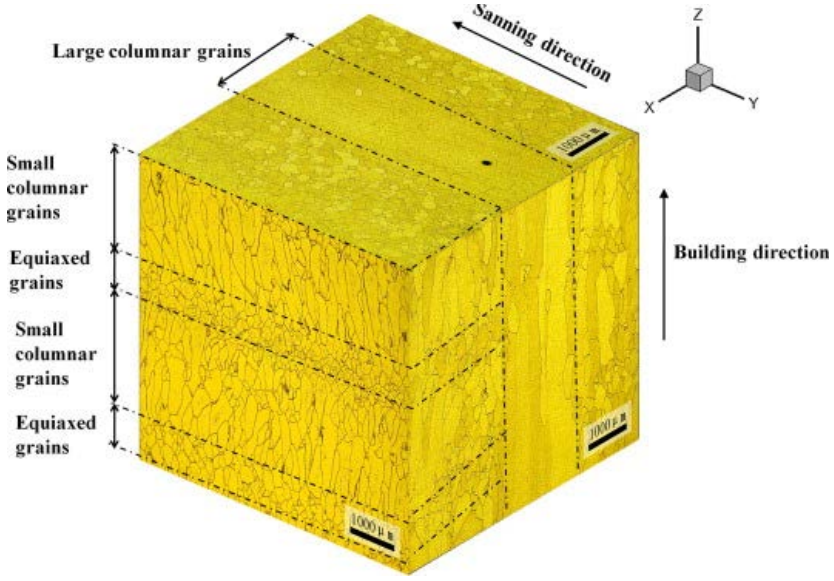

Figure 26. The "bamboo-like" grain morphology in a LP-DED Ti-5Al-5Mo-5V-1Cr-1Fe alloy [117].

Liu, *et al.* [117] studied the correlation between the microstructural evolution of a near beta titanium alloy during the LP-DED process and the part geometry (Figure 27). As can be seen in Figure 27a, during the deposition of a single track, due to the high-temperature gradient and rapid cooling at the bottom of the melt pool, the morphology of the grains is columnar. Thereafter, by increasing the melt pool height, the thermal gradient and cooling rate decrease, resulting in the transition from columnar to equiaxed at the top of the melt pool. Instead, in the case of multi-track deposition (Figure 27b), in the overlap zones, all the equiaxed grains remelt that solidify afterwards with columnar morphology. This transition in these areas is due to the lower melt pool depth in these zones that change the local thermal history in those locations. This different thermal history, particularly higher thermal gradient and cooling rates, result in columnar grain formation. In the case of multi-layer deposition, shown in Figure 27c, it is revealed that partially melted equiaxed gains of the last solidify layer to act as nuclei for the epitaxial growth of the columnar grains that have an identical morphology to the previous layer. The grain morphology in the overlapped zones, also, in this case, is as same as the multi-track deposition. However, they revealed that a variation in the LP-DED process parameters could change the grain morphologies, and so further studies regarding the effect of process parameters on the microstructural evolution are required.

Preprints (www.preprints.org) | NOT PEER-REVIEWED | Posted: 22 November 2022 doi:10.20944/preprints202211.0397.v1

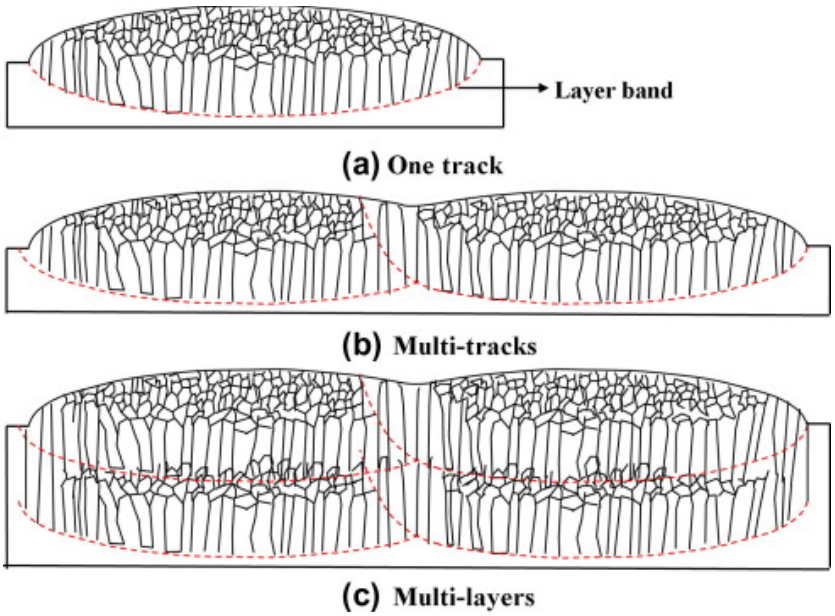

Figure 27. Schematic illustration of the microstructural evolution during the LP-DED process, (**a**) One-track, (**b**) Multi-track, and (**c**) Multi-layers [117].

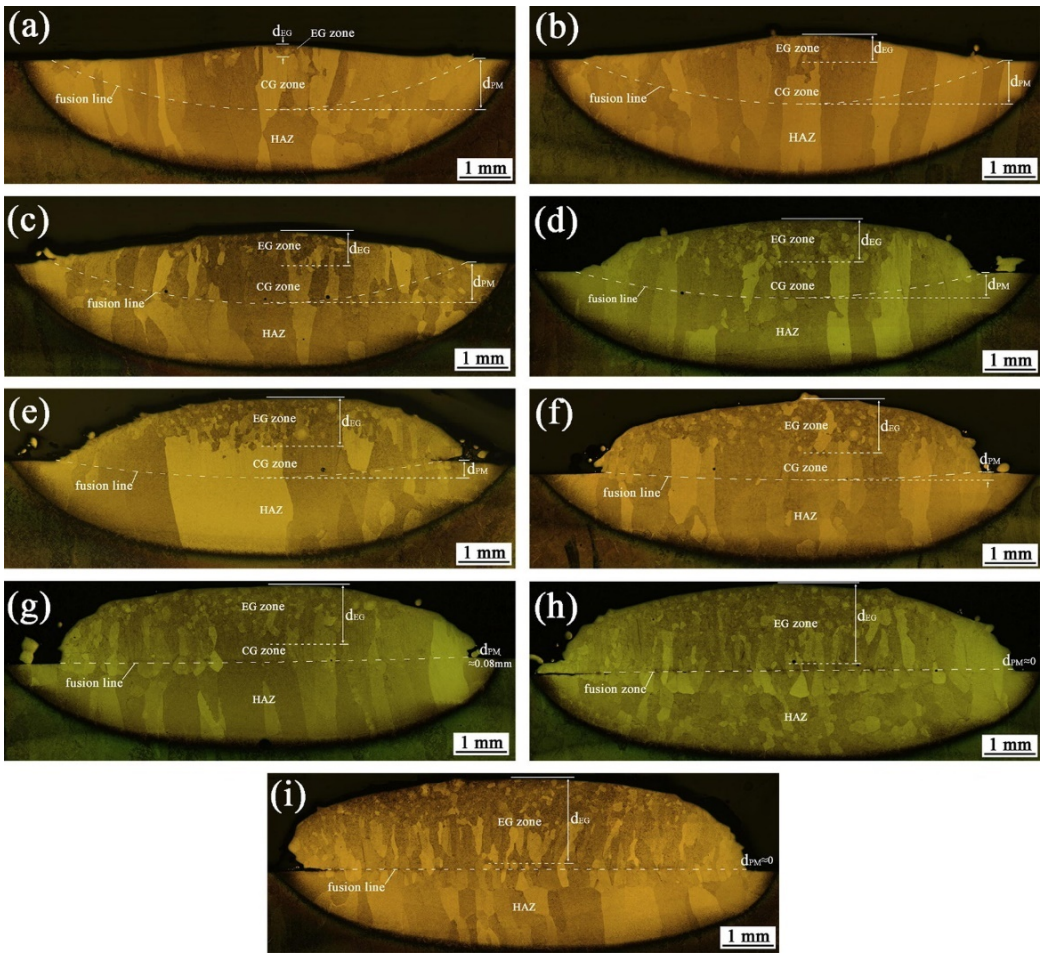

Figure 28. OM images of the cross-section of melt pools of a near beta titanium single scan tracks using (**a**) 6 g/min, (**b**) 11 g/min, (**c**) 15 g/min, (**d**) 25 g/min, (**e**) 31 g/min, (**f**) 36 g/min, (**g**) 44 g/min, (**h**) 55 g/min and (**i**) 59 g/min, as mass deposition rate [118].

 doi:10.20944/preprints202211.0397.v1

In another work, Wang, *et al.* [118] studied the effect of mass deposition rate (*m*) on the nucleation and growth mechanisms during the solidification of the melt pool in the LP-DED process. They reported that by increasing the mass deposition rate, the area fraction of the equiaxed grains increases significantly (Figure 28). In fact, by increasing the *m* value, the epitaxial growth of the parent grains is prevented more and nucleation of the new equiaxed grains increases markedly. Besides, it was revealed that higher mass deposition rates result in a lower melting pool depth, and after a critical point, no penetration occurs that is not desirable. Therefore, they concluded that through the mass deposition rate, it would be possible to change the morphology of the microstructure, but there is a critical threshold that should be respected.

Hofmeister, *et al.* [79] analysed the microstructure of 316L stainless steel thin walls. By varying the laser power, they found that a columnar microstructure was predominant near the interface, whereas a cellular microstructure was observed in the remaining regions. They observed that the dimensions of the microstructures were smaller using a low value of laser power. Mazumder, *et al.* [113] analysed the microstructure obtained from the deposition of H13 tool steel. They observed that each deposition pass was characterised by three regions: the interface region, columnar grain, and equiaxed grain region (Figure 29). The interface region corresponds to the remelted region and is characterised by a coarser mesh due to the repetitive thermal cycles. Above the interface region, the microstructures evolve to columnar grain and then to equiaxed grain, and this was attributed to a lower value of temperature gradient [113].

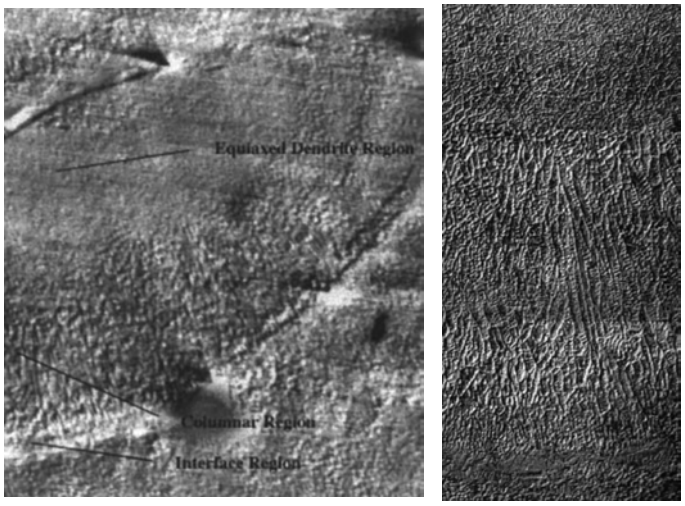

(a) **(b)**

Figure 29. (**a**) Cross-section of H13 tool steel deposit and (**b**) close-up of deposition pass characterised by three-zone: interface region, columnar region and equiaxed dendrite region [113].

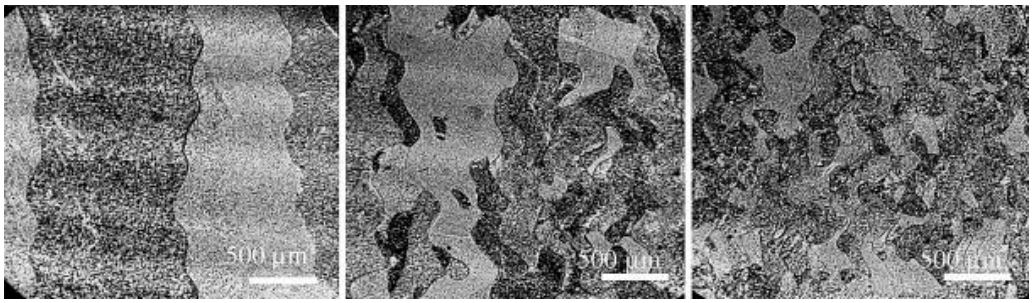

(a) **(b)** **(c)**

Figure 30. SEM micrograph showing the effect of travel speed on grain dimensions. Travel speed are: (**a**) 300 mm/min, (**b**) 600 mm/min and (**c**) 900 mm/min [119].

Preprints (www.preprints.org) | NOT PEER-REVIEWED | Posted: 22 November 2022 doi:10.20944/preprints202211.0397.v1

Mazumder, *et al.* [113] and Han, *et al.* [120] demonstrated that the microstructures were highly influenced by the process parameters. In particular, increasing the laser power and\or reducing the travel speed, coarser grains were obtained. The same behaviour was observed by Wu, *et al.* [119] for Ti-6Al-4V alloy and by Majumdar, *et al.* [121] for 316L stainless steel. Figure 30 shows the variation of grain structures dimensions obtained during the deposition of Ti-6Al-4V thin walls increasing the travel speed. Liu, *et al.* [122] deposited Inconel 718 samples on a substrate of the same material and observed that the microstructure was mainly characterised by columnar dendrites elongated along the building direction. They also observed that a finer grain structure was obtained in the overlapping regions between consecutive track, instead a coarser grain structure was obtained in the other regions (Figure 31). This was attributed to the thermal cycles that occur during the process, which in turn caused the grain recrystallisation and coarsening.

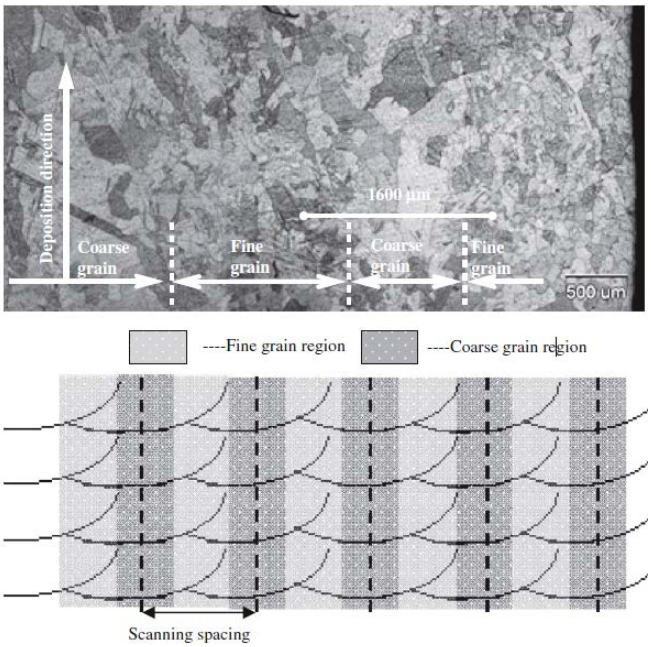

Figure 31. Cross-section of In718 deposit. Finer grain structure is observed in the overlapping regions instead coarser grain structure is observed elsewhere [122].

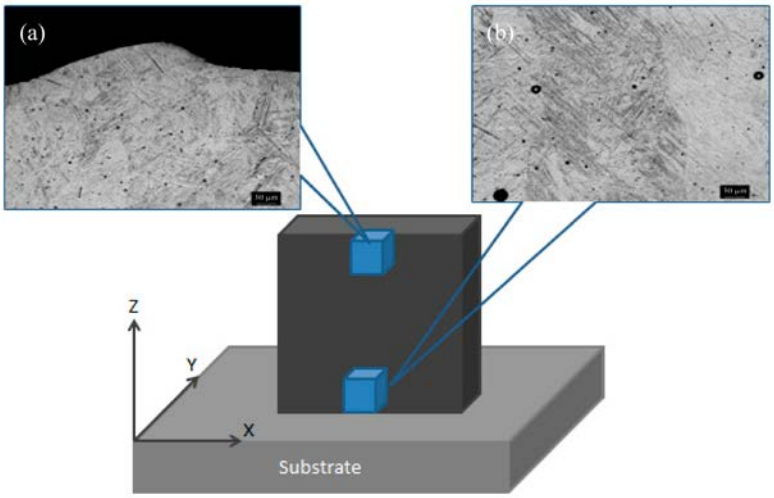

Figure 32. OM micrographs of a Ti-6Al-4V sample produced via LP-DED process from the: (**a**) top, (**b**) bottom regions [115].

 doi:10.20944/preprints202211.0397.v1

Several works have illustrated that in a metallic part produced via the LP-DED process, different local thermal gradients and cooling rates can result in the formation of various local microstructures [105,123]. For instance, in a Ti-6Al-4V component produced via LP-DED, the colonies of parallel and very fine lamellae are formed at the top of the sample in (Figure 32); in contrast, at the bottom of the sample, the lamellae become thicker [115].

4.2. Residual stress

The dynamic nature of thermal phenomena in LP-DED processes induces a high level of residual stresses. These residual stresses are developed from the reiteration of heating/cooling cycles and the high-temperature gradient during the process. According to Mercelis and Kruth [124], two mechanisms are primarily responsible for generating residual stresses: the Temperature Gradient Mechanism (TGM) and the cooling-down phase. The TGM is caused by the high-temperature gradient near the laser spot, whereas in the cooling-down phase model, the molten material shrinks during the solidification due to thermal contraction. However, this contraction is limited by the underneath material [124-126]. The magnitude of residual stresses is influenced by the material stress-strain relationship and by the strain misfit between two adjacent regions during the cooling phase [127]. In particular, higher residual stresses were observed in material characterized by a higher modulus of elasticity (E) and by a higher yield strength (Ys). For example, Rangaswamy, *et al.* [128] showed that residual stresses on the IN718 sample (E = 205 GPa, Ys = 1100 MPa) were of about 1.5 times higher than residual stresses in the 316L sample (E = 196 GPa, Ys = 450 MPa). The residual stresses in some areas can reach very high values, even 75% of the yield strength [128].

The strain misfit between adjacent regions is crucial during the production of Functionally Graded Material (FGM) in which materials with coefficients of thermal expansion (CTE) that can differ a lot are used. Woo, *et al.* [129] studied the residual stress distribution obtained in five FGM samples that produced varying chemical compositions. They observed that an abrupt variation from tension to compression occurred when the chemical composition of the samples varied.

The presence of residual stresses affects important characteristics of the produced components such as tensile and fatigue resistance, thus, the integrity and the lifetime of components are influenced [123]. Moreover, the residual stresses induce distortion [130] and loss of geometrical tolerances [131]. The stresses in the deposited material, due to complex heating and cooling cycles, assumed a highly non-uniform distribution. Rangaswamy, *et al.* [132] measured the residual stresses of two stainless steel samples using the neutron diffraction method. Samples characterised by different geometries, i.e. a thin wall and a pillar of square cross-section, were analysed. They demonstrated that a compression state was observed at the centre of each sample instead, a tension state was obtained near the edge. Later, Rangaswamy, *et al.* [128] measured the residual stress distribution of two samples with a rectangular and square cross-section using neutron diffraction and the contour method. They observed that the stresses were almost uniaxial along the building direction. Moat, *et al.* [133] analysed the stress distribution on parallelepiped samples using the contour method. Results, illustrated in Figure 33, showed that near the building platform, the stresses along the building direction were almost nil; instead, the longitudinal stresses were highly compressive. On the contrary, the stresses distribution on top layers showed that tensile stresses were obtained along the building direction, but the longitudinal stresses assumed almost zero values. This behaviour that analysed the macroscale residual stress distribution was confirmed by several authors [134-138]. Nevertheless, the high non-uniformity of residual stresses can be observed also in the mesoscale and the microscale levels, that analysed the stress distribution on layer track length scale respectively [122,139,140]. Strantza, *et al.* [139] measured the residual stresses at the mesoscale level of Ti-6Al-4V samples produced by LP-DED using the hole drilling and the slitting methods. They proved that the samples were characterised by a tensile state on the external surface that was balanced by a compression state at the centre.

 doi:10.20944/preprints202211.0397.v1

High levels of residual stresses were observed near the bottom due to the high value of the cooling rate and the cumulative effect of successive depositions. In particular, using the hole drilling strain gage method, it was observed that the residual stresses were characterized by an oscillatory nature, in which the amplitude of the oscillation is related to the layer thickness and to the hatching distance [139,141]. Using the Vickers micro-indentation method on Inconel 718 samples, Liu, *et al.* [122] showed that the higher stresses were obtained in the overlapping regions between two adjacent tracks.

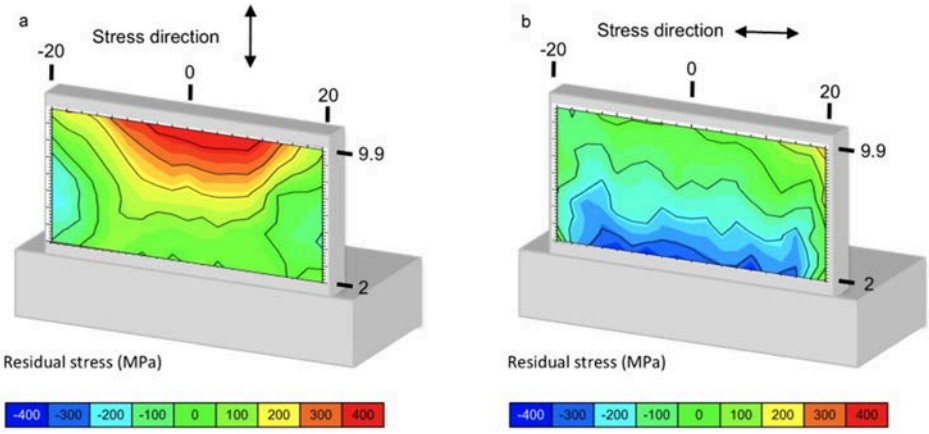

Figure 33. Residual stress distribution in Waspaloy sample (**a**) along the building direction and (**b**) along the longitudinal direction [133].

Since the residual stresses can adversely affect the mechanical performance and the functionality of the part, several efforts were performed to define methods that allow minimising the residual stresses. For this purpose, three main aspects are investigated that are the building platform temperature, the deposition strategy and the process parameters.

Based on results gained from welding processes, Chin, *et al.* [142] simulated the deposition of a single track of steel. They showed that preheating the building platform caused a reduction of the thermal gradient and residual stresses. Vasinonta, *et al.* [143] proposed a thermo-mechanical model and developed a process map to predict residual stresses. They showed that the main contribution to residual stress reduction came from the uniform preheating of the building platform. Corbin, *et al.* [144] used a laser sensor to analyse the effect of preheating temperature and building platform thickness on the deformation during the deposition of Ti6Al4V alloy. They showed that the preheating phase reduce the distortion when the thin building platform was used however, when the thick building platform was used, the preheating phase induced a higher deformation. Lu, *et al.* [130] used a Finite Element (FE) to simulate the deposition of Ti64Al4V samples. They analysed the influence of different laser paths that were used to locally increase the building platform temperature. They showed that when the local preheating was used, the residual stress value was lower with respect to the nominal case without preheating. However, the distortion increased by about 3 mm. Instead, by increasing the whole building platform temperature up to 700 °C, the residual stresses, and the distortions of Ti64Al4V samples were reduced by 80.2% and 90.1%, respectively with respect to the nominal case.

The optimization of deposition strategy is another method that is used to obtain a residual stress reduction. Dai and Shaw [145] and Nickel, *et al.* [146], using a FE model analysis, showed that the residual stresses and the related distortions depend significantly on the laser deposition strategy. Using a bi-directional deposition strategy elongated along a direction, the resulting distortion was characterised by a saddle shape (Figure 34). The distortion was reduced by varying the laser deposition pattern. In fact, using an offset-out deposition strategy (Figure 35), the induced distortion was minimised to about 1/3 compare to the distortion obtained using the first deposition pattern [145].

Preprints (www.preprints.org) | NOT PEER-REVIEWED | Posted: 22 November 2022 doi:10.20944/preprints202211.0397.v1

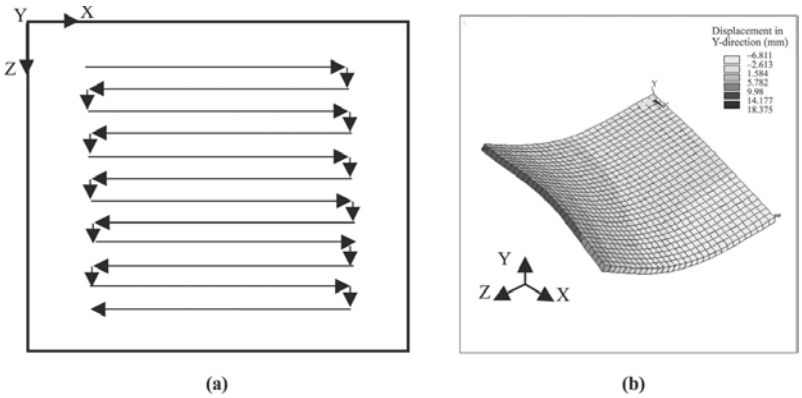

Figure 34. (**a**) Bi-directional deposition strategy and (**b**) the corresponding modelled deformation caused by residual stress [145].

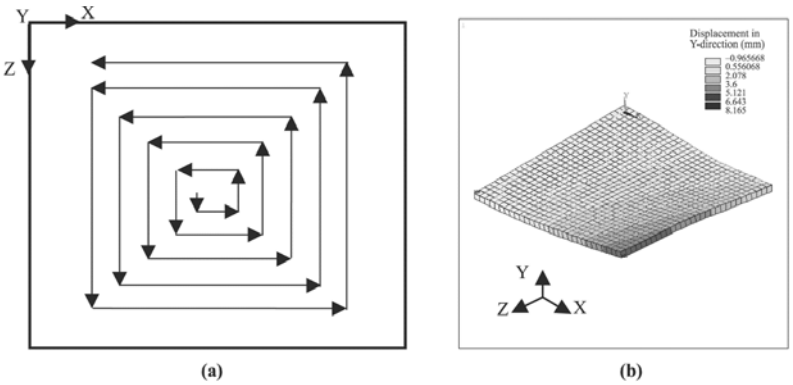

Figure 35. (**a**) Offset-out deposition strategy and (**b**) the corresponding modelled deformation caused by residual stress [145].

Saboori, *et al.* [106] compared two deposition strategies: the 0–90°, characterized by an orthogonal deposition direction between two layers, and the 0–67° that is characterized by a 67° rotation for each new layer. They showed that on the top surfaces, the residual stresses were independent from the deposition strategy; however, higher residual stresses were observed on lateral surfaces produced by the 0-90° deposition strategy. Woo, *et al.* [129] measured the residual stress in FGM samples produced with different deposition strategies. They showed that the range of stress, that is, the difference between the maximum and the minimum value, was reduced from 950 MPa to 680 MPa by rotating the deposition strategy of 90° at each layer. The lower range value of about 430 MPa was obtained using an island deposition strategy. However, using the island deposition strategy, a higher level of defects was observed.

Mitigation of residual stresses can also be obtained by varying the process parameters. In particular, lower residual stresses are obtained by varying the process parameters in order to obtain a constant melt pool dimension and a uniform temperature distribution throughout the component [128,147]. In the literature, contradictory results can be found concerning the effect of process parameters on residual stress values.

All in all, it is observed that an increase of specific energy, by increasing the laser power or reducing the travel speed, leads to an increase of residual stresses values [147-150]. Then, Balichakra, *et al.* [151], during the deposition of a γ titanium aluminide thin wall, showed that residual stresses were almost independent from the travel speed and laser power. On the other hand, anther author showed that lower residual stresses were obtained when higher laser power [152] and lower travel speed [149,152,153] were used.

 doi:10.20944/preprints202211.0397.v1

4.3. Surface quality

Components produced by the LP-DED process suffer from low surface quality. Hence, post-machining operations are required in order to achieve the dimensional and geometrical tolerances defined by the specific application. The surface quality of a component is mainly characterized by its surface roughness and dimensional accuracy [154].

Surface roughness is one of the most challenging issues in LP-DED [9,155,156]. Smugeresky, *et al.* [157] performed one of the first experimental investigations on the surface finish of samples produced by the LP-DED process. Their analysis showed that the average surface roughness (R_a) ranges between 8 and 20 μm, and the surface roughness value is mainly influenced by powder particle size. In particular, the lowest value of surface roughness was obtained when the smallest powder particle size was used. This behaviour was attributed to the presence of unmelted powder particles on the analysed surface [155]. In addition to the particle size, from the literature, it emerges that the surface roughness is highly influenced by the powder stream [158]. Based on the powder feed rate value, Resch, *et al.* [159] distinguished the surface roughness into three categories that were related to the low, the medium and the high powder feed rate value. In detail, using a low value of powder feed rate the smoother surfaces and lowest values of surface roughness were observed, but the build rate was very low. Using the higher value of powder feed the build rate increased however, the surface roughness increased significantly. Using the medium value of powder feed rate, they observed a good building rate with a reasonable surface roughness. The surface roughness is also influenced by other process parameters such as layer thickness, laser power and travel speed.

Gharbi, *et al.* [160] observed that if a thin additive layer was used in combination with an high laser power and an high travel speed, an improved surface finish was observed. This is confirmed by Peyre, *et al.* [155] that showed that by increasing the laser power, a reduction in the value of maximum surface roughness was obtained, however, the average surface roughness remained almost constant. In contrast, Mahamood, *et al.* [161] and Li, *et al.* [156] observed that average surface roughness decreased if laser power value increased. Gharbi, *et al.* [160] identified two types of roughness along the building direction (z-axis): micro-roughness and macro-waviness. The first one was attributed to the particle agglomeration in inter-layer areas and solidification line and it was mainly influenced by powder stream whereas, the macroscopic contribution, that was mostly affected by the process parameters, was related to the formation of periodic menisci, associated with the melt pool stability. In general the surface roughness can be measured on the top surface (building plane) and on the lateral surfaces (along the building direction) [162].

Despite most of the works analysed the surface roughness on the lateral surface [157,159,160,163], it is observed that surface roughness on top surfaces is slightly higher than those measured on lateral surfaces [152,164]. In particular, Piscopo, *et al.* [152] showed that the morphology of the lateral and the top surface is mainly influenced by the layer thickness and the hatching distance, respectively. In addition, analysing the morphology of the surface, described by the kurtosis and the skewness parameters, they showed that the morphology of a LP-DED sample is similar to the morphology obtained in a milling operation. In addition to the variation of process parameters, different methods are developed to improve the surface roughness. Gharbi, *et al.* [165] showed that the surface finish was improved using quasi-continuous laser irradiation instead of fully continuous laser irradiation. This was attributed to the reduction of thermal gradient and Marangoni flow in the melt pool.

One of the main methods used to reduce the surface roughness on the top surface is to scan the surface without powder feeding. This method, in analogy with the L-PBF process, is named remelting. Rombouts, *et al.* [166] studied the effect of laser remelting on surface roughness. In their work, the surface quality was evaluated in terms of the maximum height of the profile (R_t) along two directions that are parallel (X-direction) and perpendicular (Y-direction) to the deposition strategy. Before remelting, lower value of R_t

 doi:10.20944/preprints202211.0397.v1

was observed in the analysed samples. Moreover, a clear correspondence between waviness and hatching distance was identified on the as deposited samples. This correspondence was not observable after remelting. Figure 36 illustrates the surface profile data before and after remelting.

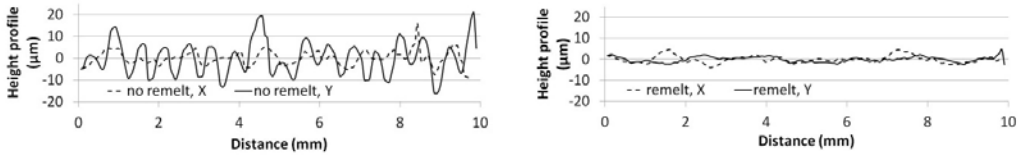

(**a**) (**b**)

Figure 36. Height profile measured on LP-DED samples (**a**) without and (**b**) with remelting [166].

The dimensional accuracy is another important factor used to describe the surface quality. In fact, based on dimensional and geometrical deviation, it is possible to design the post-processing operation [152]. Izadi, *et al.* [167] and Piscopo, *et al.* [152] reported that the dimensional deviation depends on process parameters. Gruber, *et al.* [168] on the basis of dimensional results, showed that the accuracy of the LP-DED process falls under tolerance class coarse. However, the accuracy can be increased by optimizing the process parameters [152,168]. For example, Piscopo, *et al.* [152] observed that travel speed significantly influenced dimensional deviation, that decreased as the travel speed increased. On the other hand, the dimensional deviation was not significantly influenced by laser power.

5. Conclusion

The purpose of this review is to provide a summary and analyse the physical phenomena involved during the Laser Powder Directed Energy Deposition process. First of all, it is possible to identify three mechanisms that are the powder stream process, the generation of the melt pool and the solidification process. Then, for each of these mechanisms, the most significant parameters and their effect on the analysed characteristic were analysed. The powder stream process investigated the phenomena involved in powder transport that are powder distribution, laser beam attenuation and powder temperature increment. Results showed that in the powder stream focus, the powder distribution assumed a near Gaussian distribution with powder particles concentrated in the deposition head axis. The concentration is mainly influenced by deposition head configuration and powder feed rate and deposition. The melt pool generation refers to the mechanisms that study the thermal behaviour and the convective flows within the molten material. Results highlight that high temperature gradients are obtained during the deposition process. These gradients cause convective flows of the molten material that influence the melt pool morphology. Laser power, travel speed and powder feed rate are the most significant parameters that govern the melt pool generation and evolution. The solidification of the track analyses the mechanical behaviour of the components by identifying the relationships between the process parameters and the final characteristics of the part. The main mechanical characteristics are the surface roughness, the residual stress and the microstructure. These characteristics are a consequence of the complex thermal phenomena and thermal cycles that are caused by the deposition process.

The analysis of the process has highlighted the complexity of the phenomena that occur during the deposition process and future studies are needed in order to optimize the process. Some possible activities should be focused on the development and the industrialization of new deposition head able to maximize the catchment efficiency, analyse the effect of a wider range of process parameters and a wider range of materials, investigating new deposition strategies and process parameters for residual stress reduction and finally, perform a structured analysis on dimensional and geometrical capabilities of the LP-DED process.

Author Contributions: Conceptualization, G.P., A.S., A.S., and E.A.; writing—original draft preparation, G.P., A.S., A.S., and E.A.; writing—review and editing, G.P., A.S., A.S., and E.A. All authors have read and agreed to the published version of the manuscript.

Funding: This research received no external funding.

Conflicts of Interest: The authors declare no conflict of interest.

References

1. Gibson, I.; Rosen, D.W.; Stucker, B. *Additive manufacturing technologies*. Springer: 2014; Vol. 17.
2. ASTM International. ISO/ASTM 52900:2021(E) - Standard Terminology for Additive Manufacturing – General Principles – Terminology. In *ISO/ASTM 52900:2021(E)*, ASTM International: West Conshohocken (USA), 2021.
3. Piscopo, G.; Salmi, A.; Atzeni, E. On the quality of unsupported overhangs produced by laser powder bed fusion. *International Journal of Manufacturing Research* **2019**, *14*, 198-216.
4. Wohlers, T.; Caffrey, T.; Campbell, R.I.; Diegel, O.; Kowen, J. *Wohlers Report 2022: 3D Printing and Additive Manufacturing State of the Industry; Annual Worldwide Progress Report*. Wohlers Associates: 2022.
5. Weber, C.; Peña, V.; Micali, M.; Yglesias, E.; Rood, S.; Scott, J.A.; Lal, B. The role of the national science foundation in the origin and evolution of additive manufacturing in the United States. *Science & Technology Policy Institute* **2013**, *1*.
6. Piscopo, G.; Iuliano, L. Current research and industrial application of laser powder directed energy deposition. *The International Journal of Advanced Manufacturing Technology* **2022**, *119*, 6893-6917.
7. Frazier, W.E. Metal Additive Manufacturing: A Review. *Journal of Materials Engineering and Performance* **2014**, *23*, 1917-1928.
8. ASTM International. Standard Guide for Directed Energy Deposition of Metals. PA: West Conshohocken, 2016; Vol. ASTM F3187-16.
9. Gibson, I.; Rosen, D.; Stucker, B. Directed Energy Deposition Processes. In *Additive Manufacturing Technologies*, 2015; pp 245-268.
10. Qi, H.; Mazumder, J.; Ki, H. Numerical simulation of heat transfer and fluid flow in coaxial laser cladding process for direct metal deposition. *J Appl Phys* **2006**, *100*, 024903.
11. Vilar, R. 10.07 - Laser Powder Deposition. In *Comprehensive Materials Processing*, Hashmi, S.; Batalha, G.F.; Van Tyne, C.J.; Yilbas, B., Eds. Elsevier: Oxford, 2014; pp 163-216.
12. Pinkerton, A.J. Advances in the modeling of laser direct metal deposition. *Journal of laser applications* **2015**, *27*, S15001.
13. Vetter, P.; Engel, T.; Fontaine, J. In *Laser cladding: the relevant parameters for process control*, Laser Materials Processing: Industrial and Microelectronics Applications, 1994; International Society for Optics and Photonics: pp 452-463.
14. Saboori, A.; Aversa, A.; Marchese, G.; Biamino, S.; Lombardi, M.; Fino, P. Application of Directed Energy Deposition-Based Additive Manufacturing in Repair. *Appl Sci-Basel* **2019**, *9*, 3316.
15. Kumar, S.P.; Elangovan, S.; Mohanraj, R.; Srihari, B. Critical review of off-axial nozzle and coaxial nozzle for powder metal deposition. *Materials Today: Proceedings* **2021**, *46*, 8066-8079.
16. Singh, A.; Kapil, S.; Das, M. A comprehensive review of the methods and mechanisms for powder feedstock handling in directed energy deposition. *Additive Manufacturing* **2020**, *35*.
17. Tang, Z.J.; Liu, W.W.; Wang, Y.W.; Saleheen, K.M.; Liu, Z.C.; Peng, S.T.; Zhang, Z.; Zhang, H.C. A review on in situ monitoring technology for directed energy deposition of metals. *Int J Adv Manuf Tech* **2020**, *108*, 3437-3463.
18. Naebe, M.; Shirvanimoghaddam, K. Functionally graded materials: A review of fabrication and properties. *Applied Materials Today* **2016**, *5*, 223-245.
19. Bohidar, S.K.; Sharma, R.; Mishra, P.R. Functionally graded materials: A critical review. *International Journal of Research* **2014**, *1*, 289-301.
20. Pratheesh Kumar, S.; Elangovan, S.; Mohanraj, R.; Ramakrishna, J.R. A review on properties of Inconel 625 and Inconel 718 fabricated using direct energy deposition. *Materials Today: Proceedings* **2021**, *46*, 7892-7906.
21. Sibisi, P.N.; Popoola, A.P.I.; Arthur, N.K.K.; Pityana, S.L. Review on direct metal laser deposition manufacturing technology for the Ti-6Al-4V alloy. *The International Journal of Advanced Manufacturing Technology* **2020**, *107*, 1163-1178.
22. Zhong, C.; Liu, J.; Zhao, T.; Schopphoven, T.; Fu, J.; Gasser, A.; Schleifenbaum, J.H. Laser Metal Deposition of Ti6Al4V—A Brief Review. *Applied Sciences* **2020**, *10*.
23. Lin, J.; Steen, W. Design characteristics and development of a nozzle for coaxial laser cladding. *Journal of Laser Applications* **1998**, *10*, 55-63.
24. Liu, J.; Li, L. Effects of powder concentration distribution on fabrication of thin-wall parts in coaxial laser cladding. *Optics & Laser Technology* **2005**, *37*, 287-292.
25. Pinkerton, A. Laser direct metal deposition: theory and applications in manufacturing and maintenance. In *Advances in laser materials processing*, Elsevier: 2010; pp 461-491.
26. Hoeges, S.; Zwiren, A.; Schade, C. Additive manufacturing using water atomized steel powders. *Metal powder report* **2017**, *72*, 111-117.

27. Pinkerton, A.; Li, L. Rapid prototyping using direct laser deposition—the effect of powder atomization type and flowrate. *Proceedings of the Institution of Mechanical Engineers, Part B: Journal of Engineering Manufacture* **2003**, *217*, 741-752.
28. Wallner, S. Powder Production Technologies. *BHM Berg- und Hüttenmännische Monatshefte* **2019**, *164*, 108-111.
29. Pinkerton, A.J.; Li, L. Direct additive laser manufacturing using gas- and water-atomised H13 tool steel powders. *The International Journal of Advanced Manufacturing Technology* **2004**, *25*, 471-479.
30. Anderson, I.E.; White, E.M.H.; Dehoff, R. Feedstock powder processing research needs for additive manufacturing development. *Current Opinion in Solid State and Materials Science* **2018**, *22*, 8-15.
31. Abdelwahed, M.; Bengtsson, S.; Casati, R.; Larsson, A.; Petrella, S.; Vedani, M. Effect of water atomization on properties of type 4130 steel processed by L-PBF. *Materials & Design* **2021**, *210*.
32. Pinkerton, A.J.; Li, L. Multiple-layer laser deposition of steel components using gas- and water-atomised powders: the differences and the mechanisms leading to them. *Applied Surface Science* **2005**, *247*, 175-181.
33. Pinkerton, A.J.; Li, L. Multiple-layer cladding of stainless steel using a high-powered diode laser: an experimental investigation of the process characteristics and material properties. *Thin Solid Films* **2004**, *453*, 471-476.
34. Zhong, C.; Chen, J.; Linnenbrink, S.; Gasser, A.; Sui, S.; Poprawe, R. A comparative study of Inconel 718 formed by High Deposition Rate Laser Metal Deposition with GA powder and PREP powder. *Materials & Design* **2016**, *107*, 386-392.
35. Ahsan, M.N.; Pinkerton, A.J.; Moat, R.J.; Shackleton, J. A comparative study of laser direct metal deposition characteristics using gas and plasma-atomized Ti–6Al–4V powders. *Materials Science and Engineering: A* **2011**, *528*, 7648-7657.
36. Brandt, M. *Laser Additive Manufacturing: Materials, Design, Technologies, and Applications*. Woodhead Publishing: 2016.
37. Lin, J. A simple model of powder catchment in coaxial laser cladding. *Optics & Laser Technology* **1999**, *31*, 233-238.
38. Dass, A.; Moridi, A. State of the Art in Directed Energy Deposition: From Additive Manufacturing to Materials Design. *Coatings* **2019**, *9*.
39. Lin, J. Concentration mode of the powder stream in coaxial laser cladding. *Optics & Laser Technology* **1999**, *31*, 251-257.
40. Pinkerton, A.J.; Li, L. Modelling powder concentration distribution from a coaxial deposition nozzle for laser-based rapid tooling. *Journal of Manufacturing Science and Engineering-Transactions of the Asme* **2004**, *126*, 33-41.
41. Tabernero, I.; Lamikiz, A.; Ukar, E.; De Lacalle, L.L.; Angulo, C.; Urbikain, G. Numerical simulation and experimental validation of powder flux distribution in coaxial laser cladding. *Journal of Materials Processing Technology* **2010**, *210*, 2125-2134.
42. Ibarra-Medina, J.; Pinkerton, A.J. Numerical investigation of powder heating in coaxial laser metal deposition. *Surface Engineering* **2011**, *27*, 754-761.
43. Wen, S.; Shin, Y.; Murthy, J.; Sojka, P. Modeling of coaxial powder flow for the laser direct deposition process. *International Journal of Heat and Mass Transfer* **2009**, *52*, 5867-5877.
44. Guner, A.; Bidare, P.; Jiménez, A.; Dimov, S.; Essa, K. Nozzle Designs in Powder-Based Direct Laser Deposition: A Review. *International Journal of Precision Engineering and Manufacturing* **2022**, *23*, 1077-1094.
45. Yang, N. Concentration model based on movement model of powder flow in coaxial laser cladding. *Optics & Laser Technology* **2009**, *41*, 94-98.
46. Pinkerton, A.J. An analytical model of beam attenuation and powder heating during coaxial laser direct metal deposition. *Journal of Physics D: Applied Physics* **2007**, *40*, 7323.
47. Lin, J. Numerical simulation of the focused powder streams in coaxial laser cladding. *Journal of Materials Processing Technology* **2000**, *105*, 17-23.
48. Ferreira, E.; Dal, M.; Colin, C.; Marion, G.; Gorny, C.; Courapied, D.; Guy, J.; Peyre, P. Experimental and Numerical Analysis of Gas/Powder Flow for Different LMD Nozzles. *Metals* **2020**, *10*.
49. Li, L.; Huang, Y.; Zou, C.; Tao, W. Numerical Study on Powder Stream Characteristics of Coaxial Laser Metal Deposition Nozzle. *Crystals* **2021**, *11*.
50. Ibarra-Medina, J.; Pinkerton, A.J. A CFD model of the laser, coaxial powder stream and substrate interaction in laser cladding. *Physics Procedia* **2010**, *5*, 337-346.
51. Eisenbarth, D.; Borges Esteves, P.M.; Wirth, F.; Wegener, K. Spatial powder flow measurement and efficiency prediction for laser direct metal deposition. *Surface and Coatings Technology* **2019**, *362*, 397-408.
52. Balu, P.; Leggett, P.; Kovacevic, R. Parametric study on a coaxial multi-material powder flow in laser-based powder deposition process. *Journal of Materials Processing Technology* **2012**, *212*, 1598-1610.
53. Gao, J.; Wu, C.; Liang, X.; Hao, Y.; Zhao, K. Numerical simulation and experimental investigation of the influence of process parameters on gas-powder flow in laser metal deposition. *Optics & Laser Technology* **2020**, *125*.
54. Kovalev, O.; Zaitsev, A.; Novichenko, D.; Smurov, I. Theoretical and experimental investigation of gas flows, powder transport and heating in coaxial laser direct metal deposition (DMD) process. *Journal of thermal spray technology* **2011**, *20*, 465-478.
55. Sergachev, D.; Mikhal'chenko, A.; Kovalev, O.; Kuz'min, V.; Grachev, G.; Pinaev, P. Laser-optic measurements of velocity of particles in the powder stream at coaxial laser cladding. *Physics Procedia* **2014**, *56*, 193-203.
56. Sergachev, D.V.; Mikhal'chenko, A.A.; Kovalev, O.B.; Kuz'min, V.I.; Grachev, G.N.; Pinaev, P.A. Laser-optic Measurements of Velocity of Particles in the Powder Stream at Coaxial Laser Cladding. *Physics Procedia* **2014**, *56*, 193-203.

57. Kovaleva, I.O.; Kovalev, O.B. Simulation of the acceleration mechanism by light-propulsion for the powder particles at laser direct material deposition. *Optics & Laser Technology* **2012**, *44*, 714-725.
58. Tan, H.; Zhang, F.; Wen, R.; Chen, J.; Huang, W. Experiment study of powder flow feed behavior of laser solid forming. *Optics and Lasers in Engineering* **2012**, *50*, 391-398.
59. Liu, H.; Hao, J.; Yu, G.; Yang, H.; Wang, L.; Han, Z. A Numerical Study on Metallic Powder Flow in Coaxial Laser Cladding. *Journal of Applied Fluid Mechanics* **2016**, *9*.
60. Nagulin, K.Y.; Iskhakov, F.; Shpilev, A.; Gilmutdinov, A.K. Optical diagnostics and optimization of the gas-powder flow in the nozzles for laser cladding. *Optics & Laser Technology* **2018**, *108*, 310-320.
61. Morville, S.; Carin, M.; Carron, D.; Le Masson, P.; Gharbi, M.; Peyre, P.; Fabbro, R. In *Numerical modeling of powder flow during coaxial laser direct metal deposition–comparison between Ti-6Al-4V alloy and stainless steel 316L*, Proceedings of the 2012 COMSOL Conference, Milan, 2012.
62. Thompson, S.M.; Bian, L.; Shamsaei, N.; Yadollahi, A. An overview of Direct Laser Deposition for additive manufacturing; Part I: Transport phenomena, modeling and diagnostics. *Additive Manufacturing* **2015**, *8*, 36-62.
63. Picasso, M.; Marsden, C.; Wagniere, J.; Frenk, A.; Rappaz, M. A simple but realistic model for laser cladding. *Metallurgical and Materials Transactions B* **1994**, *25*, 281-291.
64. Lin, J. Temperature analysis of the powder streams in coaxial laser cladding. *Optics & Laser Technology* **1999**, *31*, 565-570.
65. Jiazhu, W.; Liu, T.; Chen, H.; Li, F.; Wei, H.; Zhang, Y. Simulation of laser attenuation and heat transport during direct metal deposition considering beam profile. *Journal of Materials Processing Technology* **2019**, *270*, 92-105.
66. Huang, Y.-L.; Liu, J.; Ma, N.-H.; Li, J.-G. Three-dimensional analytical model on laser-powder interaction during laser cladding. *Journal of Laser Applications* **2006**, *18*, 42-46.
67. Lee, Y.; Nordin, M.; Babu, S.; Farson, D. Influence of fluid convection on weld pool formation in laser cladding. *Welding Journal* **2014**, *93*, 292S-300S.
68. Manvatkar, V.; Gokhale, A.; Reddy, G.J.; Venkataramana, A.; De, A. Estimation of melt pool dimensions, thermal cycle, and hardness distribution in the laser-engineered net shaping process of austenitic stainless steel. *Metallurgical and materials transactions A* **2011**, *42*, 4080-4087.
69. He, X.; Mazumder, J. Transport phenomena during direct metal deposition. *J Appl Phys* **2007**, *101*, 053113.
70. Unocic, R.R.; DuPont, J.N. Process efficiency measurements in the laser engineered net shaping process. *Metallurgical and Materials Transactions B* **2004**, *35*, 143-152.
71. Sears, J. In *Measuring laser absorption coefficient during laser additive manufacturing of 316L stainless steel and Ti-6V-4Al alloys*, International Congress on Applications of Lasers & Electro-Optics, 2007; LIA: p 401.
72. Peyre, P.; Aubry, P.; Fabbro, R.; Neveu, R.; Longuet, A. Analytical and numerical modelling of the direct metal deposition laser process. *Journal of Physics D: Applied Physics* **2008**, *41*, 025403.
73. Toyserkani, E.; Khajepour, A.; Corbin, S.F. *Laser cladding*. CRC press: 2004.
74. Hofmeister, W.; Griffith, M. Solidification in direct metal deposition by LENS processing. *Jom* **2001**, *53*, 30-34.
75. Zhong, M.; Liu, W. Laser surface cladding: the state of the art and challenges. *Proceedings of the Institution of Mechanical Engineers, Part C: Journal of Mechanical Engineering Science* **2010**, *224*, 1041-1060.
76. Gu, D. Laser additive manufacturing (am): classification, processing philosophy, and metallurgical mechanisms. In *Laser Additive Manufacturing of High-Performance Materials*, Springer: 2015; pp 15-71.
77. Arrizubieta, J.I.; Lamikiz, A.; Klocke, F.; Martínez, S.; Arntz, K.; Ukar, E. Evaluation of the relevance of melt pool dynamics in Laser Material Deposition process modeling. *International Journal of Heat and Mass Transfer* **2017**, *115*, 80-91.
78. Han, L.; Liou, F.W.; Musti, S. Thermal behavior and geometry model of melt pool in laser material process. *Journal of Heat Transfer* **2005**, *127*, 1005-1014.
79. Hofmeister, W.; Wert, M.; Smugeresky, J.; Philliber, J.A.; Griffith, M.; Ensz, M. Investigating solidification with the laser-engineered net shaping (LENSTM) process. *JOM* **1999**, *51*, 1-6.
80. Govekar, E.; Jeromen, A.; Kuznetsov, A.; Kotar, M.; Kondo, M. Annular laser beam based direct metal deposition. *Procedia CIRP* **2018**, *74*, 222-227.
81. Griffith, M.; Schlienger, M.; Harwell, L.; Oliver, M.; Baldwin, M.; Ensz, M.; Essien, M.; Brooks, J.; Robino, C.; Smugeresky, e.J. Understanding thermal behavior in the LENS process. *Materials & design* **1999**, *20*, 107-113.
82. Sampson, R.; Lancaster, R.; Sutcliffe, M.; Carswell, D.; Hauser, C.; Barras, J. The influence of key process parameters on melt pool geometry in direct energy deposition additive manufacturing systems. *Optics & Laser Technology* **2021**, *134*.
83. Hua, T.; Jing, C.; Xin, L.; Fengying, Z.; Weidong, H. Research on molten pool temperature in the process of laser rapid forming. *Journal of Materials Processing Technology* **2008**, *198*, 454-462.
84. Hu, Y.; Chen, C.; Mukherjee, K. Innovative laser-aided manufacturing of patterned stamping and cutting dies: Processing parameters. *Material and Manufacturing Process* **1998**, *13*, 369-387.
85. Srivastava, D.; Chang, I.; Loretto, M. The optimisation of processing parameters and characterisation of microstructure of direct laser fabricated TiAl alloy components. *Materials & Design* **2000**, *21*, 425-433.

86. Lee, E.M.; Shin, G.Y.; Yoon, H.S.; Shim, D.S. Study of the effects of process parameters on deposited single track of M4 powder based direct energy deposition. *Journal of Mechanical Science and Technology* **2017**, *31*, 3411-3418.
87. Yellup, J. Laser cladding using the powder blowing technique. *Surface and Coatings Technology* **1995**, *71*, 121-128.
88. Pinkerton, A.J.; Li, L. Modelling the geometry of a moving laser melt pool and deposition track via energy and mass balances. *Journal of Physics D: Applied Physics* **2004**, *37*, 1885.
89. Smurov, I.; Doubenskaia, M.; Grigoriev, S.; Nazarov, A. Optical Monitoring in Laser Cladding of Ti6Al4V. *Journal of Thermal Spray Technology* **2012**, *21*, 1357-1362.
90. El Cheikh, H.; Courant, B.; Branchu, S.; Hascoët, J.-Y.; Guillén, R. Analysis and prediction of single laser tracks geometrical characteristics in coaxial laser cladding process. *Optics and Lasers in Engineering* **2012**, *50*, 413-422.
91. Ocylok, S.; Alexeev, E.; Mann, S.; Weisheit, A.; Wissenbach, K.; Kelbassa, I. Correlations of melt pool geometry and process parameters during laser metal deposition by coaxial process monitoring. *Physics Procedia* **2014**, *56*, 228-238.
92. Kummailil, J.; Sammarco, C.; Skinner, D.; Brown, C.A.; Rong, K. Effect of select LENS™ processing parameters on the deposition of Ti-6Al-4V. *Journal of manufacturing processes* **2005**, *7*, 42-50.
93. Wu, X.; Zhu, B.; Zeng, X.; Hu, X.; Cui, K. Critical state of laser cladding with powder auto-feeding. *Surface and Coatings technology* **1996**, *79*, 200-204.
94. Bennett, J.L.; Wolff, S.J.; Hyatt, G.; Ehmann, K.; Cao, J. Thermal effect on clad dimension for laser deposited Inconel 718. *Journal of Manufacturing Processes* **2017**, *28*, 550-557.
95. Haley, J.C.; Schoenung, J.M.; Lavernia, E.J. Observations of particle-melt pool impact events in directed energy deposition. *Additive Manufacturing* **2018**, *22*, 368-374.
96. Limmaneevichitr, C.; Kou, S. Experiments to simulate effect of Marangoni convection on weld pool shape. *WELDING JOURNAL-NEW YORK-* **2000**, *79*, 231-S.
97. Kumar, A.; Roy, S. Effect of three-dimensional melt pool convection on process characteristics during laser cladding. *Computational Materials Science* **2009**, *46*, 495-506.
98. Yang, L.; Peng, X.; Wang, B. Numerical modeling and experimental investigation on the characteristics of molten pool during laser processing. *International journal of heat and mass transfer* **2001**, *44*, 4465-4473.
99. Kou, S. Welding metallurgy. *New Jersey, USA* **2003**, 431-446.
100. Mazumder, J. Overview of melt dynamics in laser processing. *Optical engineering* **1991**, *30*, 1208-1220.
101. Lee, Y.; Farson, D. Surface tension-powered build dimension control in laser additive manufacturing process. *The International Journal of Advanced Manufacturing Technology* **2016**, *85*, 1035-1044.
102. Tsotridis, G.; Rother, H.; Hondros, E. Marangoni flow and the shapes of laser-melted pools. *Naturwissenschaften* **1989**, *76*, 216-218.
103. Tsai, M.; Kou, S. Marangoni convection in weld pools with a free surface. *International Journal for Numerical Methods in Fluids* **1989**, *9*, 1503-1516.
104. Anthony, T.; Cline, H. Surface rippling induced by surface-tension gradients during laser surface melting and alloying. *J Appl Phys* **1977**, *48*, 3888-3894.
105. Aversa, A.; Saboori, A.; Librera, E.; de Chirico, M.; Biamino, S.; Lombardi, M.; Fino, P. The role of Directed Energy Deposition atmosphere mode on the microstructure and mechanical properties of 316L samples. *Additive Manufacturing* **2020**, *34*.
106. Saboori, A.; Piscopo, G.; Lai, M.; Salmi, A.; Biamino, S. An investigation on the effect of deposition pattern on the microstructure, mechanical properties and residual stress of 316L produced by Directed Energy Deposition. *Mat Sci Eng a-Struct* **2020**, *780*.
107. Bontha, S.; Klingbeil, N.W.; Kobryn, P.A.; Fraser, H.L. Effects of process variables and size-scale on solidification microstructure in beam-based fabrication of bulky 3D structures. *Materials Science and Engineering: A* **2009**, *513-514*, 311-318.
108. Bontha, S.; Klingbeil, N.W.; Kobryn, P.A.; Fraser, H.L. Thermal process maps for predicting solidification microstructure in laser fabrication of thin-wall structures. *Journal of Materials Processing Technology* **2006**, *178*, 135-142.
109. Lippold, J.C. *Welding metallurgy and weldability*. Wiley Online Library: 2015.
110. Steen, W.M.; Mazumder, J. *Laser material processing*. springer science & business media: 2010.
111. Selcuk, C. Laser metal deposition for powder metallurgy parts. *Powder Metallurgy* **2011**, *54*, 94-99.
112. Saboori, A.; Aversa, A.; Marchese, G.; Biamino, S.; Lombardi, M.; Fino, P. Microstructure and Mechanical Properties of AISI 316L Produced by Directed Energy Deposition-Based Additive Manufacturing: A Review. *Applied Sciences* **2020**, *10*.
113. Mazumder, J.; Schifferer, A.; Choi, J. Direct materials deposition: designed macro and microstructure. *Material Research Innovations* **1999**, *3*, 118-131.
114. Gan, Z.; Yu, G.; He, X.; Li, S. Numerical simulation of thermal behavior and multicomponent mass transfer in direct laser deposition of Co-base alloy on steel. *International Journal of Heat and Mass Transfer* **2017**, *104*, 28-38.
115. Saboori, A.; Gallo, D.; Biamino, S.; Fino, P.; Lombardi, M. An Overview of Additive Manufacturing of Titanium Components by Directed Energy Deposition: Microstructure and Mechanical Properties. *Applied Sciences* **2017**, *7*.
116. Qu, H.P.; Li, P.; Zhang, S.Q.; Li, A.; Wang, H.M. Microstructure and mechanical property of laser melting deposition (LMD) Ti/TiAl structural gradient material. *Materials & Design* **2010**, *31*, 574-582.

117. Liu, C.M.; Tian, X.J.; Tang, H.B.; Wang, H.M. Microstructural characterization of laser melting deposited Ti–5Al-5Mo–5V–1Cr–1Fe near β titanium alloy. *J Alloy Compd* **2013**, *572*, 17-24.
118. Wang, T.; Zhu, Y.Y.; Zhang, S.Q.; Tang, H.B.; Wang, H.M. Grain morphology evolution behavior of titanium alloy components during laser melting deposition additive manufacturing. *J Alloy Compd* **2015**, *632*, 505-513.
119. Wu, X.; Liang, J.; Mei, J.; Mitchell, C.; Goodwin, P.; Voice, W. Microstructures of laser-deposited Ti–6Al–4V. *Materials & design* **2004**, *25*, 137-144.
120. Han, Y.; Lu, W.; Jarvis, T.; Shurvinton, J.; Wu, X. Investigation on the microstructure of direct laser additive manufactured Ti6Al4V alloy. *Materials Research* **2015**, *18*, 24-28.
121. Majumdar, J.D.; Pinkerton, A.; Liu, Z.; Manna, I.; Li, L. Microstructure characterisation and process optimization of laser assisted rapid fabrication of 316L stainless steel. *Applied Surface Science* **2005**, *247*, 320-327.
122. Liu, F.; Lin, X.; Yang, G.; Song, M.; Chen, J.; Huang, W. Microstructure and residual stress of laser rapid formed Inconel 718 nickel-base superalloy. *Optics & Laser Technology* **2011**, *43*, 208-213.
123. Shamsaei, N.; Yadollahi, A.; Bian, L.; Thompson, S.M. An overview of Direct Laser Deposition for additive manufacturing; Part II: Mechanical behavior, process parameter optimization and control. *Additive Manufacturing* **2015**, *8*, 12-35.
124. Mercelis, P.; Kruth, J.-P. Residual stresses in selective laser sintering and selective laser melting. *Rapid prototyping journal* **2006**, *12*, 254-265.
125. Salmi, A.; Piscopo, G.; Atzeni, E.; Minetola, P.; Iuliano, L. On the Effect of Part Orientation on Stress Distribution in AlSi10Mg Specimens Fabricated by Laser Powder Bed Fusion (L-PBF). *Procedia CIRP* **2018**, *67*, 191-196.
126. Piscopo, G.; Atzeni, E.; Calignano, F.; Galati, M.; Iuliano, L.; Minetola, P.; Salmi, A. Machining induced residual stresses in AlSi10Mg component produced by Laser Powder Bed Fusion (L-PBF). *Procedia CIRP* **2019**, *79*, 101-106.
127. Withers, P.J.; Bhadeshia, H. Residual stress. Part 2–Nature and origins. *Materials science and technology* **2001**, *17*, 366-375.
128. Rangaswamy, P.; Griffith, M.L.; Prime, M.B.; Holden, T.M.; Rogge, R.B.; Edwards, J.M.; Sebring, R.J. Residual stresses in LENS® components using neutron diffraction and contour method. *Materials Science and Engineering: A* **2005**, *399*, 72-83.
129. Woo, W.; Kim, D.-K.; Kingston, E.J.; Luzin, V.; Salvemini, F.; Hill, M.R. Effect of interlayers and scanning strategies on through-thickness residual stress distributions in additive manufactured ferritic-austenitic steel structure. *Materials Science and Engineering: A* **2019**, *744*, 618-629.
130. Lu, X.; Lin, X.; Chiumenti, M.; Cervera, M.; Hu, Y.; Ji, X.; Ma, L.; Yang, H.; Huang, W. Residual stress and distortion of rectangular and S-shaped Ti-6Al-4V parts by Directed Energy Deposition: Modelling and experimental calibration. *Additive Manufacturing* **2019**, *26*, 166-179.
131. DebRoy, T.; Wei, H.L.; Zuback, J.S.; Mukherjee, T.; Elmer, J.W.; Milewski, J.O.; Beese, A.M.; Wilson-Heid, A.; De, A.; Zhang, W. Additive manufacturing of metallic components – Process, structure and properties. *Progress in Materials Science* **2018**, *92*, 112-224.
132. Rangaswamy, P.; Holden, T.; Rogge, R.; Griffith, M. Residual stresses in components formed by the laserengineered net shaping (LENS®) process. *The Journal of strain analysis for engineering design* **2003**, *38*, 519-527.
133. Moat, R.J.; Pinkerton, A.J.; Li, L.; Withers, P.J.; Preuss, M. Residual stresses in laser direct metal deposited Waspaloy. *Materials Science and Engineering: A* **2011**, *528*, 2288-2298.
134. Mukherjee, T.; Zhang, W.; DebRoy, T. An improved prediction of residual stresses and distortion in additive manufacturing. *Computational Materials Science* **2017**, *126*, 360-372.
135. Mukherjee, T.; Zuback, J.S.; Zhang, W.; DebRoy, T. Residual stresses and distortion in additively manufactured compositionally graded and dissimilar joints. *Computational Materials Science* **2018**, *143*, 325-337.
136. Li, Q.; Gnanasekaran, B.; Fu, Y.; Liu, G.R. Prediction of Thermal Residual Stress and Microstructure in Direct Laser Metal Deposition via a Coupled Finite Element and Multiphase Field Framework. *Jom* **2019**, *72*, 496-508.
137. Ghosh, S.; Choi, J. Deposition Pattern Based Thermal Stresses in Single-Layer Laser Aided Direct Material Deposition Process. *Journal of Manufacturing Science and Engineering* **2007**, *129*, 319-332.
138. Pinkerton, A.J.; Shackleton, J.; Moat, R.; Li, L.; Withers, P.; Preuss, M.; Allen, J.; Hilton, P.; Folwell, R. The effect of process parameters on residual stresses within an inconel 718 part produced by the direct laser deposition process. In *International Congress on Applications of Lasers & Electro-Optics*, 2005.
139. Strantza, M.; Vrancken, B.; Prime, M.; Truman, C.; Rombouts, M.; Brown, D.; Guillaume, P.; Van Hemelrijck, D. Directional and oscillating residual stress on the mesoscale in additively manufactured Ti-6Al-4V. *Acta Materialia* **2019**, *168*, 299-308.
140. Piscopo, G.; Atzeni, E.; Salmi, A.; Iuliano, L.; Gatto, A.; Marchiandi, G.; Balestrucci, A. Mesoscale modelling of laser powder-based directed energy deposition process. *Procedia CIRP* **2020**, *88*, 393-398.
141. Aversa, A.; Piscopo, G.; Salmi, A.; Lombardi, M. Effect of Heat Treatments on Residual Stress and Properties of AISI 316L Steel Processed by Directed Energy Deposition. *J Mater Eng Perform* **2020**.
142. Chin, R.; Beuth, J.; Amon, C. In *Control of residual thermal stresses in shape deposition manufacturing*, 1995 International Solid Freeform Fabrication Symposium, 1995.
143. Vasinonta, A.; Beuth, J.L.; Griffith, M. Process Maps for Predicting Residual Stress and Melt Pool Size in the Laser-Based Fabrication of Thin-Walled Structures. *Journal of Manufacturing Science and Engineering* **2007**, *129*, 101-109.

144. Corbin, D.J.; Nassar, A.R.; Reutzel, E.W.; Beese, A.M.; Michaleris, P. Effect of Substrate Thickness and Preheating on the Distortion of Laser Deposited Ti–6Al–4V. *Journal of Manufacturing Science and Engineering* **2018**, *140*.
145. Dai, K.; Shaw, L. Distortion minimization of laser-processed components through control of laser scanning patterns. *Rapid Prototyping Journal* **2002**, *8*, 270-276.
146. Nickel, A.; Barnett, D.; Prinz, F. Thermal stresses and deposition patterns in layered manufacturing. *Materials Science and Engineering: A* **2001**, *317*, 59-64.
147. Beuth, J.; Klingbeil, N. The role of process variables in laser-based direct metal solid freeform fabrication. *Jom* **2001**, *53*, 36-39.
148. Svetlizky, D.; Das, M.; Zheng, B.; Vyatskikh, A.L.; Bose, S.; Bandyopadhyay, A.; Schoenung, J.M.; Lavernia, E.J.; Eliaz, N. Directed energy deposition (DED) additive manufacturing: Physical characteristics, defects, challenges and applications. *Materials Today* **2021**.
149. Wang, H. Effect of Process Parameters on Residual Stress Distribution during Direct Laser Metal Deposition Shaping. *Advanced Materials Research* **2014**, *989-994*, 49-54.
150. Mirkoohi, E.; Dobbs, J.R.; Liang, S.Y. Analytical modeling of residual stress in direct metal deposition considering scan strategy. *The International Journal of Advanced Manufacturing Technology* **2020**, *106*, 4105-4121.
151. Balichakra, M.; Bontha, S.; Krishna, P.; Balla, V.K. Prediction and validation of residual stresses generated during laser metal deposition of γ titanium aluminide thin wall structures. *Materials Research Express* **2019**, *6*.
152. Piscopo, G.; Salmi, A.; Atzeni, E. Influence of High-Productivity Process Parameters on the Surface Quality and Residual Stress State of AISI 316L Components Produced by Directed Energy Deposition. *J Mater Eng Perform* **2021**, *30*, 6691-6702.
153. Wang, L.; Felicelli, S.D.; Pratt, P. Residual stresses in LENS-deposited AISI 410 stainless steel plates. *Materials Science and Engineering: A* **2008**, *496*, 234-241.
154. Cao, L.; Li, J.; Hu, J.; Liu, H.; Wu, Y.; Zhou, Q. Optimization of surface roughness and dimensional accuracy in LPBF additive manufacturing. *Optics & Laser Technology* **2021**, *142*.
155. Peyre, P.; Gharbi, M.; Gorny, C.; Carin, M.; Morville, S.; Carron, D.; Le Masson, P.; Malot, T.; Fabbro, R. In *Surface finish issues after direct metal deposition*, Materials Science Forum, 2012; Trans Tech Publ: pp 228-233.
156. Li, Y.; Yang, H.; Lin, X.; Huang, W.; Li, J.; Zhou, Y. The influences of processing parameters on forming characterizations during laser rapid forming. *Materials Science and Engineering: A* **2003**, *360*, 18-25.
157. Smugeresky, J.; Keicher, D.; Romero, J.; Griffith, M.; Harwell, L. Laser Engineered Net Shaping (LENS [TM]) Process: Optimization of Surface Finish and Microstructural Properties. *Advances in Powder Metallurgy and Particulate Materials--1997*. **1997**, *3*, 21.
158. Mahamood, R.M.; Akinlabi, E.T. Effect of Powder Flow Rate on Surface Finish in Laser Additive Manufacturing Process. *IOP Conference Series: Materials Science and Engineering* **2018**, *391*.
159. Resch, M.; Kaplan, A.F.; Schuoecker, D. In *Laser-assisted generating of three-dimensional parts by the blown powder process*, XIII International Symposium on Gas Flow and Chemical Lasers and High-Power Laser Conference, 2001; International Society for Optics and Photonics: pp 555-558.
160. Gharbi, M.; Peyre, P.; GORNY, C.; CARIN, M.; Morville, S.; LE MASSON, P.; CARRON, D.; Fabbro, R. Influence of various process conditions on surface finishes induced by the direct metal deposition laser technique on a Ti-6Al-4V alloy. *Journal of Materials Processing Technology* **2012**, *213*, 791-800.
161. Mahamood, R.M.; Akinlabi, E.T.; Shukla, M.; Pityana, S. Characterizing the effect of laser power density on microstructure, microhardness, and surface finish of laser deposited titanium alloy. *Journal of Manufacturing Science and Engineering* **2013**, *135*, 064502.
162. Mazumder, J.; Dutta, D.; Kikuchi, N.; Ghosh, A. Closed loop direct metal deposition: art to part. *Optics and Lasers in Engineering* **2000**, *34*, 397-414.
163. Gharbi, M.; Peyre, P.; GORNY, C.; Carin, M.; Morville, S.; LE MASSON, P.; CARRON, D.; Fabbro, R. Influence of a pulsed laser regime on surface finish induced by thedirect metal deposition process on a Ti64 alloy. *Journal of Materials Processing Technology* **2014**, *214*, 485-495.
164. Piscopo, G.; Salmi, A.; Atzeni, E.; Iuliano, L.; Busatto, M.; Tusacciu, S.; Lai, M.; Biamino, S.; Toushekhah, M.; Saboori, A. In *On the effect of deposition patterns on the residual stress, roughness and microstructure of AISI 316L samples produced by Directed Energy Deposition*, International Conference of Progress in Digital and Physical Manufacturing, 2019; Springer: pp 206-212.
165. Gharbi, M.; Peyre, P.; Gorny, C.; Carin, M.; Morville, S.; Le Masson, P.; Carron, D.; Fabbro, R. Influence of various process conditions on surface finishes induced by the direct metal deposition laser technique on a Ti–6Al–4V alloy. *Journal of Materials Processing Technology* **2013**, *213*, 791-800.
166. Rombouts, M.; Maes, G.; Hendrix, W.; Delarbre, E.; Motmans, F. Surface finish after laser metal deposition. *Physics Procedia* **2013**, *41*, 810-814.
167. Izadi, M.; Farzaneh, A.; Mohammed, M.; Gibson, I.; Rolfe, B. A review of laser engineered net shaping (LENS) build and process parameters of metallic parts. *Rapid Prototyping Journal* **2020**, *26*, 1059-1078.
168. Gruber, S.; Grunert, C.; Riede, M.; López, E.; Marquardt, A.; Brueckner, F.; Leyens, C. Comparison of dimensional accuracy and tolerances of powder bed based and nozzle based additive manufacturing processes. *Journal of Laser Applications* **2020**, *32*.